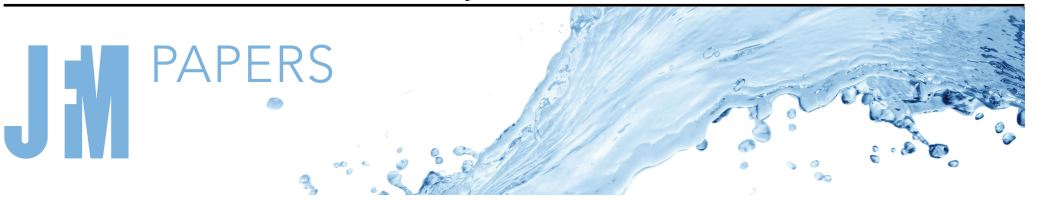
J. Fluid Mech. (2026), *vol.* 1037, A46, doi:10.1017/jfm.2026.11642



Finite-Reynolds-number effects on the structure functions in turbulent flow with external intermittency

Yuanliang Xie[1], **Kun Wu**[2], **Xue-Lu Xiong**[1], **Koji Nagata**[3], **Tomoaki Watanabe**[3] **and Yi Zhou**[1]

[1]School of Energy and Power Engineering, Nanjing University of Science and Technology, Nanjing 210094, PR China

[2]State Key Laboratory of High Temperature Gas Dynamics, Institute of Mechanics, Chinese Academy of Sciences, Beijing 100190, PR China

[3]Department of Mechanical Engineering and Science, Kyoto University, Kyoto 615-8540, Japan

Corresponding authors: Kun Wu, wukun@imech.ac.cn; Yi Zhou, yizhou@njust.edu.cn

(Received 14 November 2025 UTC; revised 15 April 2026 UTC; accepted 29 April 2026 UTC)

High-resolution direct numerical simulation data of a turbulent plane jet at Reynolds numbers $Re_H = 10^4$ and 10^5, based on the nozzle width, are employed to investigate the behaviour of the structure functions in the flow region with external intermittency. In the intermittent turbulent region, the conditional second-order longitudinal and transverse structure functions exhibit self-similar behaviour at small and intermediate scales. Moreover, as the order increases from the second to the sixth, the conditional higher even-order structure function profiles progressively deviate from self-similarity and the predictions of Kolmogorov's universal equilibrium theory. The conditional third-order structure function only displays self-similarity within the small-scale dissipation range, albeit the range of self-similarity extends to progressively larger values of r/η^T for a higher Reynolds number, where η^T denotes conditional Kolmogorov length scale and r is the separation distance. As the intermittency factor decreases, the unsteady term in the Kármán–Howarth equation becomes more significant, leading to a larger deviation from Kolmogorov's 4/5 law. The extrapolation results based on the empirical formula for the structure function $\langle \delta u'^n \rangle(r)$ indicate that the finite-Reynolds-number effect on the structure function may differ between the intermittent and fully turbulent regions. The structure functions in the intermittent region may follow the predictions of K41 theory, i.e. $\langle \delta u'^n \rangle(r) \sim r^{n/3}$, which is consistent with the results observed in the fully turbulent region. However, the realisation of Kolmogorov's predictions is more difficult in the intermittent region than in the fully turbulent region and requires a much higher local Reynolds

© The Author(s), 2026. Published by Cambridge University Press.

https://doi.org/10.1017/jfm.2026.11642 Published online by Cambridge University Press

number. It is further found that the conditional third-order structure function profiles recover self-similarity at intermediate scales when the local Reynolds number exceeds 10^5. These findings provide valuable insights into the understanding and modelling of mixing transition problems.

Key words: free shear layers, turbulent flows, intermittency

1. Introduction

In the classical Richardson–Kolmogorov view of the energy cascade, also known as the K41 theory (Kolmogorov 1941*a*,*b*,*c*), fully developed turbulent flows at sufficiently high Reynolds numbers consist of eddies covering a wide range of scales. The kinetic energy is transferred from larger to smaller scales. The K41 theory was derived based on the similarity framework, and is known for its simplicity and elegance. Based on the first and second similarity hypotheses, Kolmogorov (1941*b*) derived the two-thirds law for the second-order longitudinal structure function (LSF) $\langle \delta u'^2 \rangle(r)$ in the inertial range, that is,

$$\left\langle \delta u'^2 \right\rangle(r) = C_2^{LSF} \varepsilon^{2/3} r^{2/3}, \tag{1.1}$$

where $\delta u'(r) = u'(\boldsymbol{x} + r\boldsymbol{e}_1) - u'(\boldsymbol{x})$ represents the velocity increment between points $\boldsymbol{x} + r\boldsymbol{e}_1$ and $\boldsymbol{x}$. Here, $\boldsymbol{e}_1$ and r are the unit vector of the streamwise direction and the separation distance along the unit vector direction, respectively, C_2^{LSF} is a Kolmogorov (universal) constant for $\langle \delta u'^2 \rangle(r)$ (Pope 2000; Davidson 2004), and ε is the kinetic energy dissipation rate. In the same year, Kolmogorov (1941*a*) also derived a simple expression for $\langle \delta u'^3 \rangle(r)$ (hereafter referred to as the Kolmogorov 4/5 law) from the transport equation of $\langle \delta u'^2 \rangle(r)$, expressed as $\langle \delta u'^3 \rangle(r) = -4/5\varepsilon r$. The Kolmogorov 4/5 law reflects the mean rate and direction of energy transfer toward smaller scales at a scale r within the inertial range. While this law is widely regarded as strictly valid for stationary isotropic turbulence at infinite Reynolds number, it has not yet been fully verified by experimental or direct numerical simulation (DNS) studies (Tang *et al.* 2019).

Considering the large-scale fluctuations in energy dissipation, the shortcoming of the simplified K41 theory was predicted by Landau & Lifshits (1944) at an early stage, foreseeing the absence of a universal form for the structure of turbulence in the inertial range. A refined K62 theory (Kolmogorov 1962) that abandons the concept of local universality has been proposed to account for the variation in ε induced by large-scale motions. The K62 theory accounts for the deviations of the scaling exponents from the K41 predictions by taking small-scale intermittency into consideration. Extensive studies (both experimental (Stolovitzky, Kailasnath & Sreenivasan 1992; Stolovitzky & Sreenivasan 1994; Lawson *et al.* 2019) and numerical (Wang *et al.* 1996; Schumacher, Sreenivasan & Yakhot 2007; Yao *et al.* 2024)) have been performed and provided evidence supporting the K62 theory in fully turbulent flows, particularly based on results from the atmospheric surface layer (Obukhov 1962). However, recent studies have suggested that there is no reason to abandon K41 (Sreenivasan & Dhruva 1998; Antonia & Burattini 2006; Antonia *et al.* 2017; Tang *et al.* 2017, 2019; Antonia *et al.* 2019*a*,*b*). One reason is that both the K41 and K62 theories rely on the assumption of an infinite Reynolds number. However, experimental evidence supporting anomalous scaling of the structure function (Sreenivasan & Antonia 1997) has not fully accounted for finite-Reynolds-number (FRN) effects. Ishihara *et al.* (2009, 2016) investigated the three-dimensional energy spectrum of

https://doi.org/10.1017/jfm.2026.11642 Published online by Cambridge University Press

stationary forced periodic box turbulence over a wide range of Re_λ (=167–2297) and found that the spectrum exhibits clear FRN effects. Furthermore, significant FRN effects have also been observed in other turbulence statistics, such as structure functions (Tang *et al.* 2017; Antonia *et al.* 2019*a*; Tang *et al.* 2023) and pressure spectra (Tsuji & Ishihara 2003). One interesting finding is that these statistical results appear to increasingly approach the K41 asymptotes as the Reynolds number increases.

In both nature and engineering, a common flow phenomenon is the turbulent flow region, separated from the non-turbulent flow region by a thin shear layer called the turbulent/non-turbulent interface (TNTI) (da Silva *et al.* 2014). The separation between turbulent and non-turbulent regions indicates large-scale fluctuations in energy production and dissipation, and leads to characteristic features of external intermittency near the turbulent boundary (LaRue & Libby 1976; Sreenivasan 1991). A comprehensive understanding of external intermittency is crucial for modelling the mixing transition problem (Wang & Fu 2011; Xie *et al.* 2025*a*) in practical engineering applications. However, until now, investigations of FRN effects on structure functions have focused on the fully turbulent region, while the influence of external intermittency has been significantly overlooked. One remaining important question is whether the conditional second-order structure function in the intermittent region follows the classical $2/3$ scaling law, while the conditional third-order structure function satisfies the Kolmogorov $4/5$ law. This paper focuses on FRN effects on structure functions in the intermittent region due to the presence of the TNTI.

Davidson (2004) and Monin & Yaglom (2007) proposed a simple two-state model (strong dissipation and weak dissipation states) based on K41 theory to explain the effect of large-scale inhomogeneities on small-scale universality. Despite lacking a solid theoretical foundation, this model has also been used to roughly predict the Kolmogorov constant with large-scale energy injection (Chien, Blum & Voth 2013). However, a recent study by Watanabe *et al.* (2019*a*) suggested that non-equilibrium dissipation occurs near the TNTI at relatively low Reynolds numbers, where Taylor's dissipation law does not apply. Turbulence near the TNTI layer exhibits pronounced large-scale inhomogeneity and anisotropy at relatively low Reynolds numbers (da Silva *et al.* 2014; Zecchetto & da Silva 2021). This suggests that the direct application of this model to the intermittent region may be limited, as turbulence in this region may exist in two different states. In contrast, turbulence near the TNTI layer becomes more isotropic at higher Reynolds numbers, as demonstrated by the analysis of the anisotropy tensors of Reynolds stress and vorticity (Zhang, Watanabe & Nagata 2023). Therefore, the two-state model also needs to take into account Reynolds number dependence when applied to the intermittent region. This is necessary to explain the variation of the Kolmogorov constant with the intermittency factor γ.

The influence of large-scale motions on the small scales causes the second-order structure function to change from flow to flow (Blum *et al.* 2011). Recently, it has been demonstrated that an extended $2/3$ power law holds for the second-order structure function in the developing region of various grid-generated turbulence (e.g. regular grid, fractal-square grid, singe-square grid), clearly violating the well-known K41 theory (Laizet, Vassilicos & Cambon 2013; Zhou *et al.* 2016; Alves Portela, Papadakis & Vassilicos 2017). Alves Portela *et al.* (2017) and Zhou *et al.* (2019, 2020) pointed out that the energy spectrum exhibits the classical approximate $-5/3$ scaling law in the intermittency region associated with large-scale vortex shedding. The key to explaining the appearance of the $-5/3$ spectrum lies in the phenomenological model that within the intermittent flow region, the turbulent components in the dissipation and intermediate ranges exhibit similarity properties akin to those in fully turbulent flows (Zhou *et al.* 2023). Zhou *et al.*

https://doi.org/10.1017/jfm.2026.11642 Published online by Cambridge University Press

(2023) further indicate that the universal constant C_{k1} in spectral space exhibits a clear power-law dependence on the intermittency factor γ, i.e. $C_{k1} \sim \gamma^{1/3}$. A parallel study was recently carried out in the intermittent region to examine the emergence of the 2/3 scaling law in the inertial range of the structure function (Xie *et al.* 2025*b*). The results indicate that the universal constant C_2^{LSF} in physical space exhibits the same dependence on γ, i.e. $C_2^{LSF} \sim \gamma^{1/3}$. However, the existence of the TNTI induces blocking/sheltering mechanism (Hunt & Durbin 1999; da Silva *et al.* 2014), causing the structure function to exhibit unique behaviour near TNTI (Xie *et al.* 2025*b*). Compared with second-order structure functions, higher-order structure functions are highly sensitive to the effect of external intermittency (Gauding *et al.* 2021). Another pertinent question concerns the self-similarity of higher-order structure functions in the intermittent region, as well as the effect of the TNTI blocking/sheltering mechanism on their self-similar behaviour.

The objective of this study is to investigate the aforementioned questions within the framework of a temporally evolving turbulent plane jet. In particular, we focus on the FRN effect of the second- and third-order structure functions in the intermittent region. Note that the different flow types (e.g. the temporally evolving jet, the spatially evolving jet and spatially evolving round jet) are expected to lead to distinctly different growth behaviour (van Reeuwijk, Vassilicos & Craske 2021; Er, Laval & Vassilicos 2023). More specifically, the temporally developing self-similar turbulent jet conserves volume flux. In contrast, the spatially developing jet conserves momentum flux. This means that applying similar analytical methods in this paper to spatially evolving jets (e.g. the spatially evolving round jet), which are of more practical interest, requires careful consideration. The remainder of the paper is organised as follows. In § 2, we provide a concise overview of the numerical methods and parameters employed for simulating the temporally evolving turbulent plane jet. A simplified two-state model based on K41 theory is used to investigate the self-similarity of the structure functions, as discussed in § 3. In § 4, the self-similarity of the third-order structure function and the contribution of the unsteady term are further examined. The FRN effect on the structure functions in the intermittent and fully turbulent regions is discussed in § 5. In § 6, we highlight the main findings and propose potential avenues for future research.

2. Numerical details and turbulence characteristics of the turbulent plane jet

2.1. *Numerical details and computational parameters*

In this study, the three-dimensional data from prior DNS studies of the temporally evolving turbulent jet performed by Watanabe *et al.* (2019*b*) and Hayashi *et al.* (2021) are used to investigate the effects of external intermittency on the second- and third-order structure functions. In the streamwise X and spanwise Z directions, periodic boundary conditions are imposed and uniformly distributed spacings are used. In the normal Y direction, a free-slip boundary condition is applied and the grid is stretched using a mapping function (Watanabe *et al.* 2019*b*). The spatial derivatives are discretised using the fully conservative central difference scheme proposed by Morinishi *et al.* (1998). A second-order scheme is applied in the normal Y direction, while fourth-order difference schemes are applied in the streamwise X and spanwise Z directions. A third-order Runge–Kutta method is employed for the time advancement and the Bi-CGSTAB method is adopted to solve the pressure Poisson equation. Nagarajan, Lele & Ferziger (2003) and Suzuki *et al.* (2013) quantified the errors in the first- and second-order derivatives, and higher-order statistics of the fourth-order and second-order fully conservative finite difference schemes using Fourier analysis. The results indicate that each term in the Reynolds-stress transport equation

https://doi.org/10.1017/jfm.2026.11642 Published online by Cambridge University Press

Re_H	N_s	θ_0/H	L_X/H	L_Y/H	L_Z/H	N_X	N_Y	N_Z	$\Delta X/\eta$	$\Delta Y/\eta$	$\Delta Z/\eta$	Re_λ
10^4	6	1/100	6	10	4	864	1200	576	1.5	1.2	1.5	100
10^5	1	1/100	6	10	4	4608	5800	3072	1.7	1.5	1.7	353

Table 1. Numerical parameters for the DNS of temporally evolving turbulent plane jets. The turbulence statistics at $T/T_{ref} = 20.0$, including $\Delta X/\eta$, $\Delta Y/\eta$, $\Delta Z/\eta$ and Re_λ, are computed at the centre plane of the jet.

shows good agreement with the corresponding results obtained using spectral methods. For a more detailed examination of the errors associated with the finite difference schemes adopted, please refer to Appendix A of Watanabe *et al.* (2018*a*).

The initial streamwise velocity component of a turbulent jet is given by the hyperbolic tangent function (da Silva & Pereira 2008; Hayashi, Watanabe & KNagata 2021), while the normal and spanwise velocity components are set to zero. Considering that the Reynolds number significantly affects the behaviour of structure functions (Pearson & Antonia 2001), the present study uses two different cases to investigate the effects of external intermittency on the longitudinal and transverse structure functions. Although high-fidelity and high-resolution three-dimensional DNS data are obtained using state-of-the-art massively parallel computations, the Reynolds number remains limited. Therefore, the influence of small-scale intermittency and the related anomalous scaling is not considered in the present study. The global Reynolds number based on the initial streamwise velocity U_{in} along the centreline and the jet width H is defined as $Re_H = U_{in}H/\nu$, and takes the values 10^4 and 10^5. The corresponding mesh numbers are $N_X \times N_Y \times N_Z = 864 \times 1200 \times 576$ and $N_X \times N_Y \times N_Z = 4608 \times 5800 \times 3072$, respectively. The numerical parameters of DNS are summarised in table 1 and a schematic of the DNS of the turbulent plane jet is shown in figure 1. It is well known that the computational cost of temporally evolving flows is significantly lower than that of spatially evolving flows at the same Reynolds number. In other words, temporally evolving flows often provide a more feasible approach for accessing data at higher Reynolds numbers. Furthermore, for the temporally evolving jet, the ensemble averages are taken over the two homogeneous directions (i.e. the streamwise and spanwise directions), which enables the statistical results to converge readily. Another motivation for selecting the jet configuration arises from our previous studies showing that the second-order structure function in the developing region of spatially evolving wakes is significantly affected by large-scale strong vortex shedding. The observed power-law exponent is 1, which is significantly larger than the classical value of 2/3. Therefore, it is a reasonable choice to use a temporally evolving plane jet for this investigation. However, a significant limitation of temporally evolving flows is the limited number of spatial samples available in a single instantaneous field. This makes it difficult to obtain statistically converged results, particularly for higher-order statistics such as the third-order structure function. For this reason, the DNS is performed N_S times for each Reynolds number Re_H using different initial velocity perturbations, where the values of N_S are listed in table 1. Note that the strength of the random initial perturbations is consistent and the root mean square (r.m.s.) magnitude of the perturbations is equal to 2.5 % of the initial mean streamwise velocity at the centre plane. The mean streamwise velocity and the r.m.s. velocity components in all three directions were examined, which showed reasonably good agreement with previous numerical simulations and experimental data. For further description of the numerical validation, one can refer to Watanabe *et al.* (2019*b*) and Hayashi *et al.* (2021).

https://doi.org/10.1017/jfm.2026.11642 Published online by Cambridge University Press

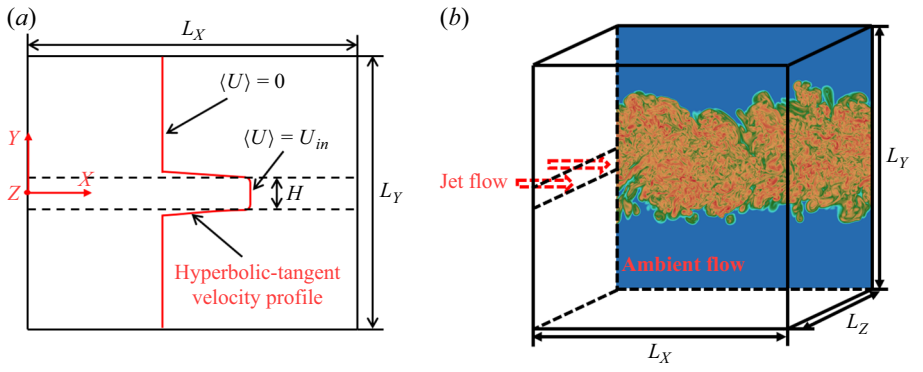


Figure 1. Schematic of the DNS of a turbulent plane jet. (*a*) Two-dimensional initial velocity field in the X–Y plane; (*b*) three-dimensional computational domain together with a randomly chosen vorticity field in the X–Y plane. The initial jet parameters are also shown, where H denotes the initial jet width and U_{in} denotes the initial centreline velocity of the jet.

Since the thickness of the TNTI is comparable to the Kolmogorov scale (Watanabe *et al.* 2018*b*; Zhang, Watanabe & Nagata 2018), high spatial resolution is required for accurate numerical studies of external intermittency. In the centre plane of the jet, the normalised spatial resolutions in the X and Y directions are $\Delta X/\eta = 1.5$, $\Delta Y/\eta = 1.2$ for $Re_H = 10^4$ and $\Delta X/\eta = 1.7$, $\Delta Y/\eta = 1.5$ for $Re_H = 10^5$ at $T/T_{ref} = 20.0$, where $\eta = (\nu^3/\varepsilon)^{1/4}$ represents the Kolmogorov length scale and $\varepsilon = 2\nu\langle s_{ij}s_{ij}\rangle$ is the kinetic energy dissipation rate. Note that the normalised spatial resolutions in the X and Z directions are identical, i.e. $\Delta X/\eta = \Delta Z/\eta$. The local Reynolds numbers, Re_λ, is calculated using the Taylor microscale $\lambda = u_{rms}/\sqrt{\langle(\partial u'/\partial x)^2\rangle}$ and the r.m.s. velocity u_{rms} of the streamwise component along the centre plane of the jet. For $Re_H = 10^4$ and 10^5, these values remain approximately constant after reaching the fully developed state at 100 and 353, respectively. Here, the angled brackets $\langle\rangle$ denote the ensemble average of statistical quantities over the X–Z plane, taking into account the flow symmetry in the Y direction. The spatial resolution and turbulent Reynolds number are also presented in table 1.

2.2. *Large-scale and small-scale intermittency of the turbulent plane jet*

Before exploring the second- and third-order structure functions of the intermittent region, the identification of the outer edge of the TNTI layer is briefly discussed. Following previous studies on TNTI, an isosurface of vorticity threshold $|\boldsymbol{\omega}| = |\boldsymbol{\omega}|_{th}$ is used to detect the outer edge of the TNTI. The specific value of $|\boldsymbol{\omega}|_{th}$ is determined by the sensitivity of the detected turbulent volume fraction V_T to $|\boldsymbol{\omega}|_{th}$ (not shown herein for economy of space). Consistent with previous studies by Hayashi *et al.* (2021) and Xie *et al.* (2025*b*), the vorticity threshold $|\boldsymbol{\omega}|_{th} = 0.01\langle|\boldsymbol{\omega}|\rangle_C$ was chosen to identify the outer edge of the TNTI, where the subscript C denotes the value at the centre plane of the jet.

Figure 2 visualises the colour contour of the vorticity magnitude $|\boldsymbol{\omega}|$ and the outer edge of the TNTI on an X–Z plane at the cross-wise position $Y/b_U = 1.6$. Here, b_U indicates the jet half-width, defined as the distance from the centreplane where the mean streamwise velocity falls to half of its value at the centreplane. The highly contorted outer edge of the TNTI can be characterised by the multiscale turbulent motions occurring under the TNTI layer over a wide range of length scales. Therefore, the turbulent region at $Re_H = 10^5$ exhibits finer vorticity structures and smaller characteristic length scales compared with

https://doi.org/10.1017/jfm.2026.11642 Published online by Cambridge University Press

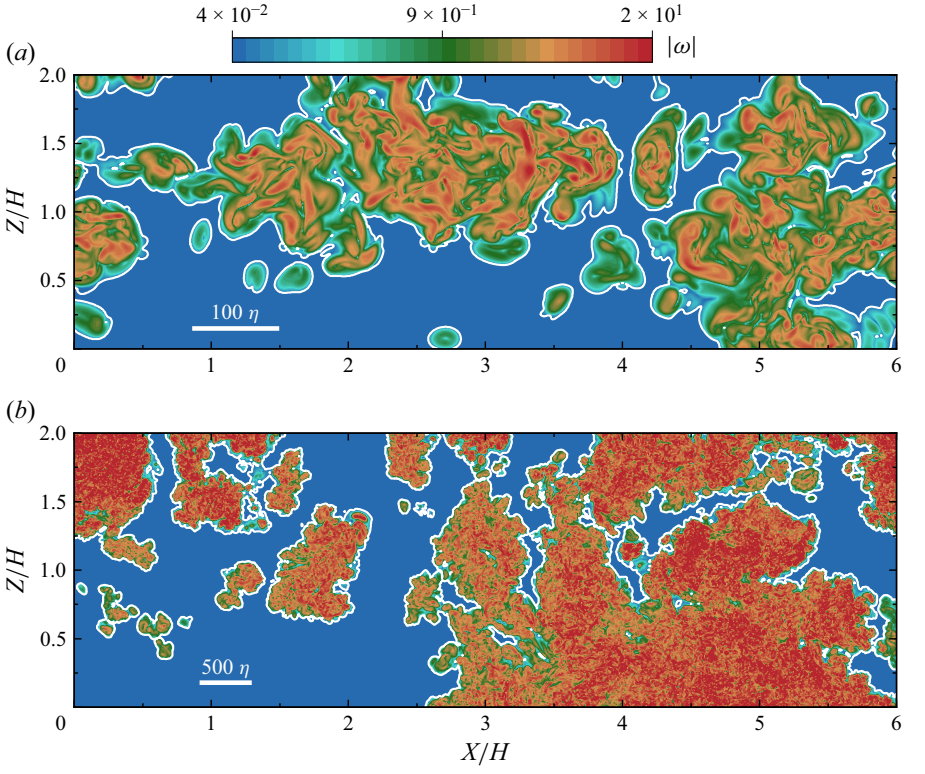


Figure 2. Logarithmic contours of the vorticity magnitude $|\boldsymbol{\omega}|$ at the cross-wise position $Y/b_U = 1.6$. The solid white line indicates the outer edge of the TNTI, which is defined by the vorticity threshold $\omega_{th} = 0.01\langle|\boldsymbol{\omega}|\rangle_C$. (*a*) $Re_H = 10^4$; (*b*) $Re_H = 10^5$. Note that only a part of the computational domain in the X–Z plane is plotted. For reference, the white bar in the lower left corner represents 100 and 500 times the Kolmogorov length scale of the jet centre plane.

that at $Re_H = 10^4$. It should be mentioned that the outer edge of TNTI appears to be relatively smooth, similar to previous observations in turbulent jets (da Silva *et al.* 2014; Watanabe *et al.* 2019*a*). This implies that the vorticity threshold selected in the present DNS effectively distinguishes between the turbulent and non-turbulent regions.

As can be seen from figure 2, the temporally evolving plane turbulent jet is a typical intermittent flow and exhibits distinct external intermittency near the TNTI. Once the outer edge of the TNTI is detected, conditional statistics related to the intermittency of the flow can be computed. Figure 3(*a*) shows the vertical distribution of the intermittent factor γ at two different Reynolds numbers. Here, the intermittent factor γ is defined as the probability that a fluid point is in a turbulent region at a fixed cross-wise position (Zhou *et al.* 2020; Hayashi *et al.* 2021). By definition, $\gamma = 1$ for a fully turbulent region, whereas $\gamma = 0$ for a non-turbulent region. It can be seen that the vertical distribution of the intermittency factor γ is almost independent of the Reynolds number when normalised by b_U. Specifically, for the flow region with $Y/b_U \leqslant 0.8$, the flow is always turbulent, while it is intermittent in the region with $0.8 \leqslant Y/b_U \leqslant 2.5$, as shown in figure 3(*a*).

Reuther & Kähler (2020) revealed that the traditional averaging methods combine information from both laminar and turbulent flows in the intermittent region, which affects the statistics of small-scale turbulence. Therefore, the applicability of the traditional averaging method in intermittent regions is questionable. For this reason,

https://doi.org/10.1017/jfm.2026.11642 Published online by Cambridge University Press

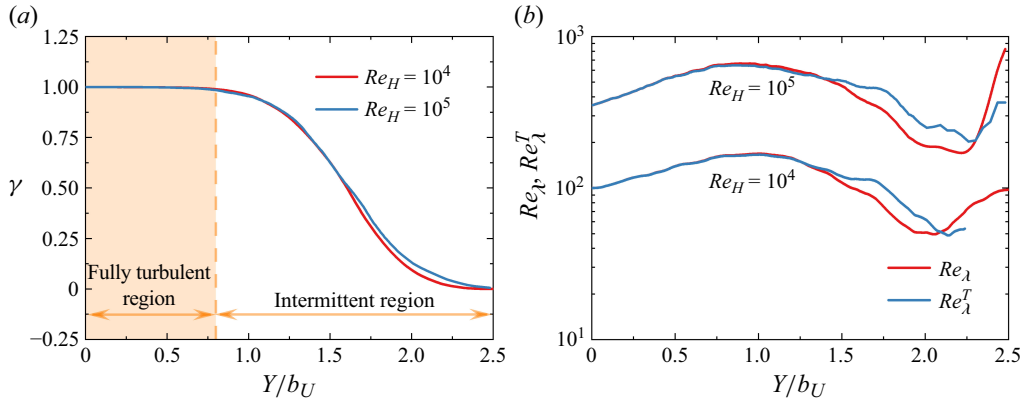


Figure 3. (*a*) Vertical distribution of the intermittency factors γ; (*b*) vertical distributions of the turbulent Reynolds number for a fully developed state. In panel (*a*), the vertical dashed line separates the fully turbulent region from the intermittent region. In panel (*b*), Re_λ denotes the traditional averaged value, while Re_λ^T denotes the conditionally averaged value in the turbulent region.

a conditional averaging method based on the intermittency factor γ is employed to analyse the turbulence characteristics within intermittent regions (Kovasznay, Kibens & Blackwelder 1970). In particular, for any statistical variable f, the traditional average value can be expressed as a weighted average of two different flow states, that is, $f = \gamma f^T + (1-\gamma) f^L$. Here, the superscripts T and L denote the ensemble averages in the turbulent and laminar regions, respectively. The vertical distributions of local Reynolds number Re_λ and the corresponding conditional local Reynolds number Re_λ^T are shown in figure 3(*b*). Note that Re_λ^T is calculated by $Re_\lambda^T = u_{rms}^T \lambda^T / \nu$, where u_{rms}^T and $\lambda^T = u_{rms}^T / \sqrt{((\partial u'/\partial x)^2)^T}$ denote the r.m.s. velocity and Taylor microscale in the turbulent region, respectively. For the fully turbulent region with $\gamma = 1$ (corresponding to $Y/b_U \leqslant 0.8$), the local Reynolds number increases continuously along the normal direction. The maximum value of Re_λ occurs at approximately $Y/b_U = 1.0$. Considering that both the mean shear $\partial U/\partial Y$ and the r.m.s. velocity fluctuations (Hayashi *et al.* 2021; Xie *et al.* 2024) tend to reach their maximum at this location, this finding is expected. For the intermittent region with $1.0 \leqslant Y/b_U \leqslant 2.0$, both Re_λ and Re_λ^T decrease monotonically, with Re_λ^T being significantly larger than Re_λ, as it should be. Note that a higher conditional local Reynolds number Re_λ^T in the intermittent region is observed over a wide range of intermittency compared with the fully turbulent jet centre plane. This results from the fact that in the intermittent region with lower γ values, although u_{rms}^T is relatively smaller, λ^T increases significantly and dominates the overall trend.

The large-scale intermittency of the flow in the intermittent region was evaluated by the skewness $S(u') = \langle u'^3 \rangle / \langle u'^2 \rangle^{3/2}$ and flatness $F(u') = \langle u'^4 \rangle / \langle u'^2 \rangle^2$ of the velocity fluctuations (Xie *et al.* 2025*b*). The results show that large-scale motions in the intermittent region are highly intermittent, with $F(u')$ up to 9 and $S(u')$ around 2, deviating significantly from the Gaussian values ($F(u') = 3.0$, $S(u') = 0.0$). In this study, the skewness $S(\partial u'/\partial X)$ and flatness $F(\partial u'/\partial X)$ of the velocity derivative are further investigated to explore small-scale intermittency in the intermittent region. The skewness and flatness of the velocity derivative as a function of the cross-wise position are shown in figure 4. It can be observed that $S(\partial u'/\partial X)$ is almost independent of Re_H, whereas $F(\partial u'/\partial X)$ increases with increasing Re_H in the fully turbulent region. On the centreplane of the jet, the skewness $S(\partial u'/\partial X)$ is nearly identical at the two Reynolds numbers

https://doi.org/10.1017/jfm.2026.11642 Published online by Cambridge University Press

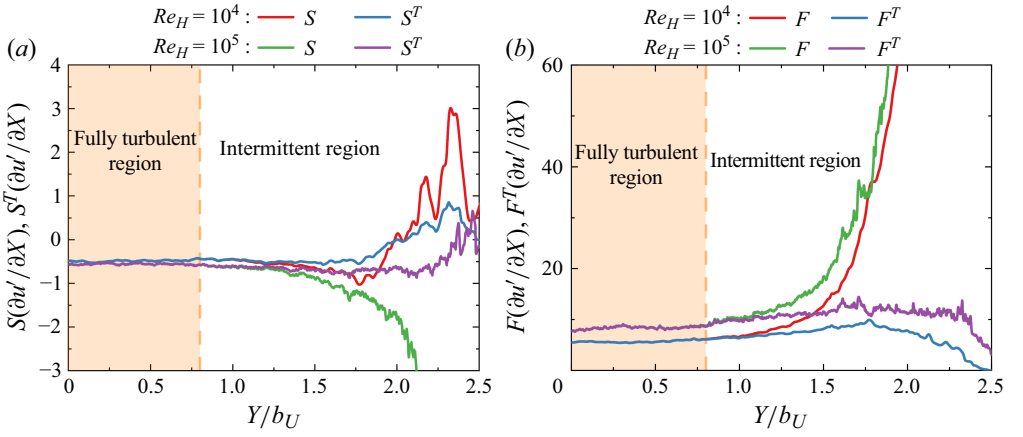


Figure 4. Vertical distributions of (*a*) the skewness, $S(\partial u'/\partial X)$ and $S^T(\partial u'/\partial X)$, and (*b*) the flatness, $F(\partial u'/\partial X)$ and $F^T(\partial u'/\partial X)$, of the streamwise velocity derivative for two different Reynolds numbers. The vertical dashed line separates the fully turbulent region from the intermittent region.

($Re = 10^4$ and 10^5), with a value of approximately -0.57, while $F(\partial u'/\partial X)$ are 5.51 and 7.52, respectively. These values are consistent with the previous research results on small-scale intermittency at comparable local Reynolds numbers (Van Atta & Antonia 1980; Kerr 1985; Kitamura *et al.* 2014). One interesting finding is that the skewness $S^T(\partial u'/\partial X)$ and flatness $F^T(\partial u'/\partial X)$ of the conditional velocity derivative remain approximately constant in the region with $Y/b_U \leqslant 1.5$. This observation supports the argument of Zhou *et al.* (2023) that the turbulent motions in the intermittent region exhibit characteristics similar to those in fully turbulent flows.

3. Conditional structure functions in a highly intermittent flow

3.1. *Self-similarity of the conditional second-order structure functions*

Townsend (1951) proposed that turbulence in most shear flows reaches a self-similar state after the flow becomes fully developed. In this state, the profiles of certain turbulence statistics exhibit reasonably good collapses when normalised by a set of characteristic length and velocity scales. The recent work by Xie *et al.* (2025*b*) investigated the self-similar behaviour of the conditional second-order structure function in the intermittent region, following the self-similarity observed in the conditional energy spectrum (Zhou *et al.* 2023). The results indicate that the distribution of the conditional longitudinal structure function exhibits self-similarity at small and intermediate scales when properly normalised using the conditional Kolmogorov scale. The presence of self-similarity implies that the conditional longitudinal structure function can be described using a single similarity variable (Xie *et al.* 2025*b*), i.e.

$$\langle \delta u'^2 \rangle(\zeta) / \left(\gamma \nu_\eta^{T2} \right) = g(\zeta), \tag{3.1}$$

where $\zeta = r/\eta^T$ represents the single similarity variable and ν_η^T denotes the conditional Kolmogorov velocity scale. Note that the difference between the standard and conditional structure functions lies in the choice of normalisation parameters. Therefore, their overall shapes are expected to be the similar. The self-similar conditional second-order longitudinal structure function further allows the derivation of the scaling law for the

https://doi.org/10.1017/jfm.2026.11642 Published online by Cambridge University Press

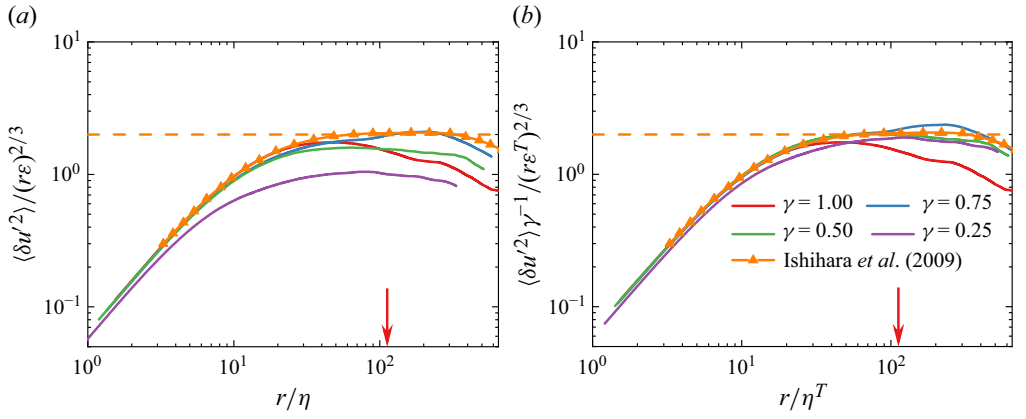


Figure 5. (*a*) Second-order longitudinal structure function, normalised by the Kolmogorov length scale η and the averaged dissipation rate ε, and (*b*) the corresponding conditional longitudinal structure function, normalised by the conditional Kolmogorov length scale η^T and the conditional energy dissipation rate ε^T, of the streamwise velocity fluctuations at four different cross-wise positions for $Re_H = 10^4$. The horizontal dashed line shows the asymptotic value of the Kolmogorov constant C_2^{LSF} as the Reynolds number approaches infinity. For comparison, the distribution of structure functions is compared with DNS data for isotropic turbulence with $Re_\lambda = 257$ (Ishihara, Gotoh & Kaneda 2009). The vertical arrow indicates the location corresponding to the integral length scale L at the jet centre plane.

Kolmogorov constant C_2^{LSF} in the intermittent region, namely

$$C_2^{LSF} = \gamma^{1/3} C_2^{LSF,\,Cond}, \tag{3.2}$$

where C_2^{LSF} and $C_2^{LSF,\,Cond}$ are the Kolmogorov constant and the conditional Kolmogorov constant, respectively. Here, C_2^{LSF} and $C_2^{LSF,\,Cond}$ are determined by the structure function and conditional structure function, respectively. A more detailed derivation of the conditional second-order structure function and the scaling law for the Kolmogorov constant C_2^{LSF} can be found in Appendix B of Xie *et al.* (2025*b*). According to the local isotropic assumption, the conditional transverse second-order structure function (TSF) will exhibit self-similar behaviour. This self-similar behaviour is accompanied by a power-law scaling between the prefactor C_2^{TSF} of $\langle \delta v'^2 \rangle(r)$ and the intermittency factor γ, that is, $C_2^{TSF} = \gamma^{1/3} C_2^{TSF,\,Cond}$. In Appendix A, a simplified two-state model effectively establishes the connection between the Kolmogorov constants C_2^{LSF} and C_2^{TSF} and γ.

In this section, we further investigate the Reynolds number dependence of the self-similarity of the structure function in the intermittent region. Figures 5 and 6 show the normalised longitudinal structure function and the corresponding conditional longitudinal structure function at four different cross-wise positions (i.e. $\gamma = 0.25$, 0.50, 0.75 and 1.00) for two different Reynolds numbers. The statistical convergence of the ensemble average is discussed in Appendix B. The vertical arrow indicates the location corresponding to the integral length scale L at the jet centre plane, where L is determined by the integral of the velocity auto-correlation function. Numerical integration of the velocity auto-correlation function shows that L is approximately 112η and 638η for the two different Reynolds numbers ($Re_H = 10^4$ and 10^5), respectively. Furthermore, the jet half-width b_U is approximately 200η and 1062η, respectively.

For the jet centre plane with $\gamma = 1.0$, the distribution of structure functions shows good agreement with the results of isotropic turbulence at similar Reynolds numbers. Kolmogorov's universal equilibrium theory suggests that the statistical properties of

https://doi.org/10.1017/jfm.2026.11642 Published online by Cambridge University Press

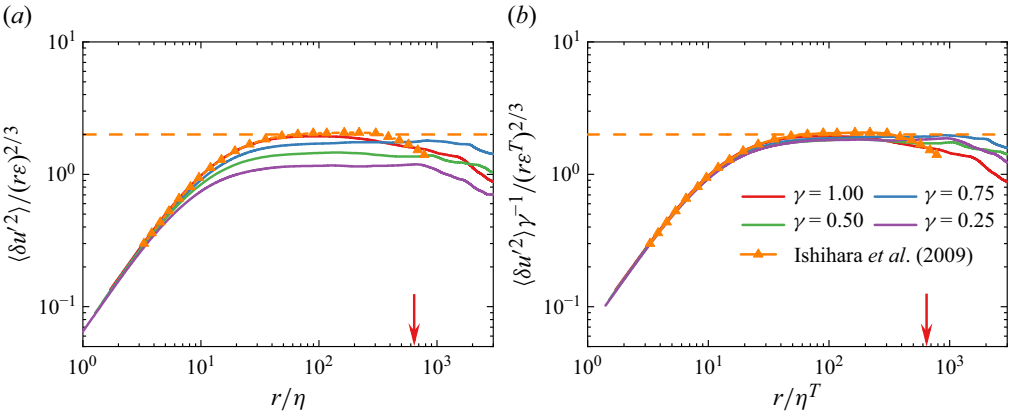


Figure 6. Same as figure 5, but for $Re_H = 10^5$.

turbulence become independent of the flow type and specific location for the small-scale dissipation range, and follow the classical Kolmogorov scaling law: $\langle \delta u'^2 \rangle(r)/v_\eta^2 \propto (r/\eta)^2$. The good collapse of the structure functions at $r/\eta \leqslant 8$ in figures 5(*a*) and 6(*a*) shows good agreement with the theory, except for the highly intermittent region of $\gamma = 0.25$ at the lower Reynolds number $Re_H = 10^4$. The present results provide insights into the statistical properties of small-scale turbulence in the intermittent region. It is worth noting that the conditional structure functions are identical to the normal structure functions, with the only difference arising from the normalisation parameters. Therefore, the general profile of the conditional structure function in the intermittent region is unaffected by patch size.

Figures 5(*b*) and 6(*b*) show the corresponding conditional longitudinal structure functions for two different Reynolds numbers. It can be observed that the conditional longitudinal structure function profiles at different cross-wise positions reasonably collapse at small and intermediate scales. A previous study (Xie *et al.* 2025*b*) has shown that the distribution of the conditional second-order longitudinal structure function deviates from self-similarity in the highly intermittent region of $\gamma = 0.25$ at the lower Reynolds number $Re_H = 40000$. This slight deviation has been attributed to the blocking/sheltering mechanisms of TNTI (Hunt & Durbin 1999; da Silva *et al.* 2014), since the turbulence near the TNTI layer is characterised by the large-scale inhomogeneity and anisotropy (da Silva *et al.* 2014; Zecchetto & da Silva 2021). This result is consistent with the current findings for the lower Reynolds number, as shown in figure 5(*b*). For a higher Reynolds number $Re_H = 10^5$, however, the slight deviation from the self-similarity of the conditional structure function is not observed (see figure 6*b*). This behaviour may be related to the turbulence near the TNTI layer tending to become more isotropic at the higher Re_H, as demonstrated by the analysis of the anisotropy tensors of Reynolds stress and vorticity (Zhang *et al.* 2023). Finally, it should also be mentioned that the reasonable collapse of the conditional structure function in the intermediate range implies that the scaling law of the Kolmogorov constant C_2^{LSF} (i.e. $C_2^{LSF} \sim \gamma^{1/3}$) is independent of the Reynolds number within the currently investigated range. Therefore, the scaling law of Kolmogorov constant C_2^{LSF} derived from the K41 theoretical framework may be considered robust, at least for the two simulations considered.

The longitudinal structure function is related to the energy dissipation, while the transverse structure function reflects the characteristics of the enstrophy field. Numerous studies (Dhruva, Tsuji & Sreenivasan 1997; Shen & Warhaft 2002; Grauer, Homann & Pinton 2012; Iyer, Sreenivasan & Yeung 2017) have shown that the longitudinal and

https://doi.org/10.1017/jfm.2026.11642 Published online by Cambridge University Press

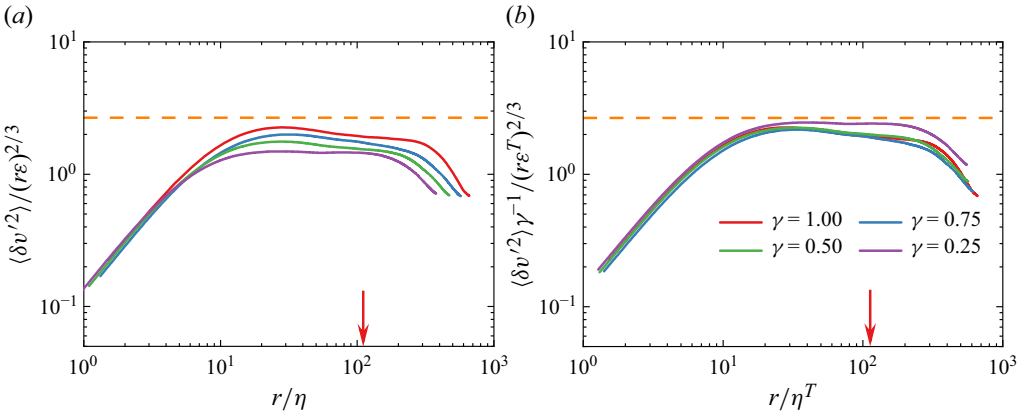


Figure 7. (*a*) Second-order transverse structure function, normalised by the Kolmogorov length scale η and the averaged dissipation rate ε, and (*b*) the corresponding conditional transverse structure function, normalised by the conditional Kolmogorov length scale η^T and the conditional energy dissipation rate ε^T, of the normal velocity fluctuations at four different cross-wise positions for $Re_H = 10^4$. The horizontal dashed line shows the asymptotic value of the Kolmogorov constant C_2^{TSF} as the Reynolds number approaches infinity, i.e. $\langle \delta v'^2 \rangle (r)/(\varepsilon r)^{2/3} = 2.67$ (Pope 2000). The vertical arrow indicates the location corresponding to the integral length scale L at the jet centre plane.

transverse structure functions are different. One notable difference is that the scaling exponent of the transverse structure function is always smaller than that of the longitudinal structure function, although the K41 theory predicts identical scaling exponents for both. It is not surprising that different physical fields exhibit distinct degrees of intermittency. So far, universal relations between the longitudinal and transverse structure functions have been established in the fully turbulent region. To assess the local isotropy of turbulence, further analysis has been conducted on the transverse structure function. The normalised second-order transverse structure function, and the corresponding conditional transverse structure function are plotted in figures 7 and 8 for two different Reynolds numbers. It can be seen from figures 7(*a*) and 8(*a*) that the shape of the structure function appears to remain almost unchanged across four different cross-wise positions. This observation somewhat echoes the argument by Kuznetsov, Praskovsky & Sabelnikov (1992) that the external intermittency induced by TNTI primarily affects the Kolmogorov constant without altering the scaling exponent of the structure function. For a higher Reynolds number Re_H, the Kolmogorov constant C_2^{TSF} in the fully turbulent region approaches the theoretical value of infinite Reynolds number. Moreover, in the intermittent region, the Kolmogorov constant C_2^{TSF} decreases as the intermittent factor γ decreases.

The corresponding conditional transverse structure functions for the two different Reynolds numbers are shown in figures 7(*b*) and 8(*b*). For four different cross-wise positions, profiles of the conditional transverse structure function exhibit self-similarity at small and intermediate scales. For the higher Reynolds number case in figure 8(*b*), a more satisfactory collapse is observed. This means that the turbulent properties in the intermittent region are similar to those of the fully turbulent flow. This idea was first proposed by Zhou *et al.* (2023) in spatially evolving wakes to explain the presence of a non-Kolmogorov –5/3 spectra (Zhou *et al.* 2019) in the highly intermittent region. It is worth noting that, although the turbulence statistics related to structure functions are shown only in log–log scales, we confirm that the reported findings are not sensitive to different coordinate scales (e.g. linear–log scale). Therefore, our conclusions are expected

https://doi.org/10.1017/jfm.2026.11642 Published online by Cambridge University Press

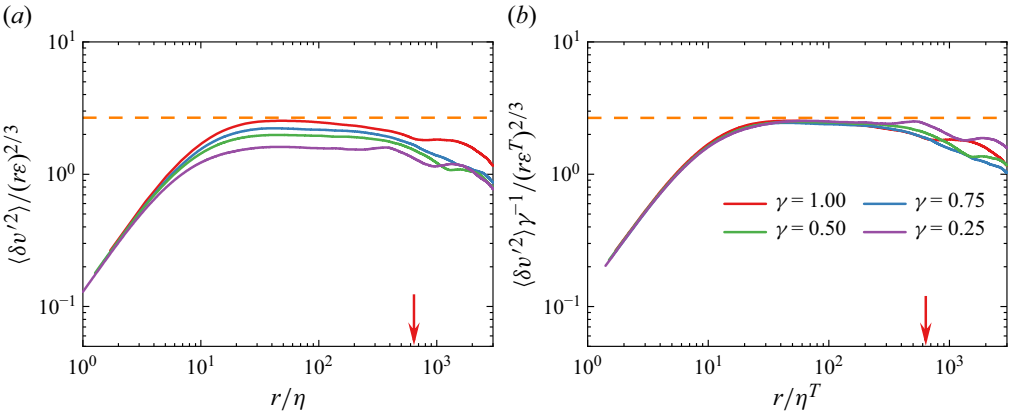


Figure 8. Same as figure 7, but for $Re_H = 10^5$.

to be robust, especially for the current higher Reynolds number (not shown herein for economy of space).

Another probably interesting finding is that, compared with the fully turbulent region with $\gamma = 1.0$, the intermittent region exhibits significant mean shear, which is expected to affect the behaviour of the structure functions, at least to some extent (Thiesset, Antonia & Djenidi 2014; Sadeghi, Lavoie & Pollard 2015). Here, the mean shear effect on the structure functions is further investigated through the Corrsin scale (Corrsin 1958). The Corrsin scale is obtained by equating the eddy-turnover time scale to the mean-shear time scale, yielding $L_c = (\varepsilon/S^3)^{1/2}$, where $S = \partial U/\partial Y$. The Corrsin scale separates the region dominated by mean shear ($r > L_c$) from the inertial region ($r < L_c$). Therefore, the onset of shear-affected scales may be characterised by $r = L_c$, as reported by Rosa (2026). Based on theoretical analysis, mean shear effects do not have a significant influence on the behaviour of the energy spectrum over the corresponding wavenumber range when $kL_c \gg 8^{-1/2}$, where k represents the angular wavenumber. However, the theoretical criterion $kL_c \gg 8^{-1/2}$ does not provide a clearly defined numerical threshold. This criterion remains somewhat ambiguous when used to quantitatively characterise the influence of mean shear on the structure functions. According to the experimental findings of Saddoughi & Veeravalli (1994) at high Reynolds numbers, the influence of mean shear on the energy spectrum can be considered negligible when $kL_c > 3$. Correspondingly, the mean shear does not affect the behaviour of the structure functions when the separation scale $r < 2\pi L_c/3$ in physical space. Saddoughi & Veeravalli (1994) further concluded that the inertial subrange remains unaffected by mean shear only when the condition $S_c^* = S(\nu/\varepsilon)^{1/2} \ll 1$ is satisfied, where S_c^* denotes the ratio of the Kolmogorov to mean-shear time scales. It should be noted that these conclusions apply only at higher Reynolds numbers.

To quantitatively assess the mean shear effects, the Corrsin scale L_c and the related shear parameters for three intermittent regions for the higher Reynolds number case of $Re_H = 10^5$ are summarised in table 2. In this study, the inertial subrange is determined to be within the range of $r/\eta^T = 60.0$ to 100.0. Table 2 implies that the scale-dependent shear parameter $2\pi L_c^T/3$ ranges from $238\eta^T$ to $307\eta^T$, which is significantly larger than the separation scale r considered in the structure function analysis. Furthermore, the conditional ratio $S^T(\nu/\varepsilon^T)^{1/2}$ remains below 0.043 in three intermittent regions, which is much smaller than 1. These quantitative results confirm that the mean shear effect is not strong enough to reach the inertial range. As shown in figures 6(*b*) and 8(*b*), differences

https://doi.org/10.1017/jfm.2026.11642 Published online by Cambridge University Press

γ	L_c	L_c^T	$2\pi L_c/3$	$2\pi L_c^T/3$	$S(\nu/\varepsilon)^{1/2}$	$S^T(\nu/\varepsilon^T)^{1/2}$
0.75	140η	$123\eta^T$	293η	$257\eta^T$	0.037	0.041
0.50	204η	$147\eta^T$	427η	$307\eta^T$	0.029	0.036
0.25	266η	$144\eta^T$	557η	$238\eta^T$	0.024	0.043

Table 2. Turbulence statistics associated with mean shear at three intermittent regions.

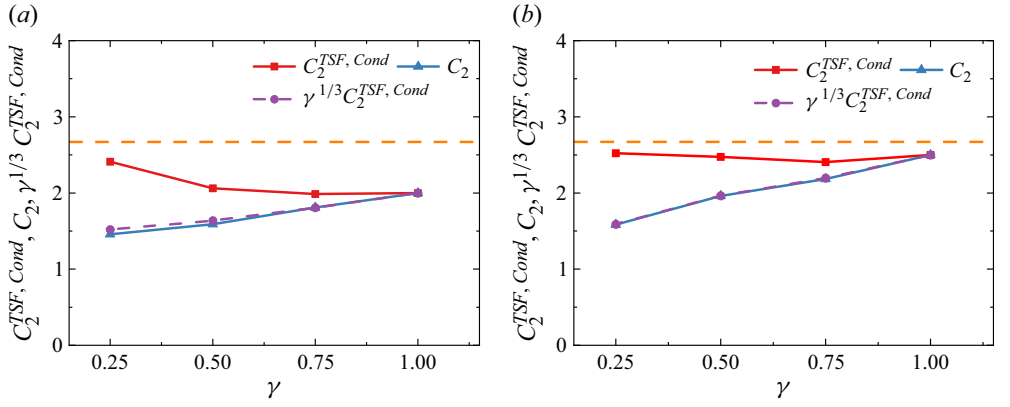


Figure 9. Kolmogorov constant C_2^{TSF} and conditional Kolmogorov constant $C_2^{TSF,\,Cond}$ as a function of intermittency factors γ within the inertial subrange for two different Reynolds numbers. For comparison, the profile of $\gamma^{1/3}C_2^{TSF,\,Cond}$ is also plotted. (*a*) $Re_H = 10^4$, (*b*) $Re_H = 10^5$. The horizontal dashed line shows the asymptotic value of the Kolmogorov constant C_2^{TSF} as the Reynolds number approaches infinity, i.e. $\langle \delta v'^2 \rangle(r)/(\varepsilon r)^{2/3} = 2.67$ (Pope 2000).

in the structure function profiles can only be found at large scales, which suggests that the influence of mean shear on the structure functions at small and intermediate scales can be negligible. Conversely, for lower Reynolds numbers, the mean shear effect may extend into the inertial range of the structure functions to some extent.

The scaling law $C_2^{LSF} = \gamma^{1/3}C_2^{LSF,\,Cond}$ for $\langle \delta u'^2 \rangle(r)$ has been evaluated and shows fairly good agreement with the intermittency factor γ (Xie *et al.* 2025*b*). To evaluate the scaling law $C_2^{TSF} = \gamma^{1/3}C_2^{TSF,\,Cond}$ for $\langle \delta v'^2 \rangle(r)$, figure 9 presents the Kolmogorov constant C_2^{TSF}, and conditional Kolmogorov constant $C_2^{TSF,\,Cond}$ and $\gamma^{1/3}C_2^{TSF,\,Cond}$ versus the intermittency factor γ. The self-similar behaviour of the conditional transverse structure functions at intermediate scales implies that $C_2^{TSF,\,Cond}$ is approximately constant, i.e. $C_2^{LSF} \sim \gamma^{1/3}$. The inertial subrange is selected to lie within the range $r/\eta^T = 60-100$, where the second-order structure function exhibits a distinct plateau region (see figures 7 and 8). It can be observed from figure 9 that the scaling law $C_2^{TSF} \sim \gamma^{1/3}$ holds roughly throughout the intermittent region. Moreover, the scaling law for the Kolmogorov constant C_2^{TSF} is influenced by the Reynolds number. For a higher Reynolds number $Re_H = 10^5$, the scaling law $C_2^{TSF} \sim \gamma^{1/3}$ becomes more consistent. In summary, these findings confirm that the scaling law of the Kolmogorov constant for $\langle \delta v'^2 \rangle(r)$ can be considered robust, particularly at higher Reynolds numbers.

https://doi.org/10.1017/jfm.2026.11642 Published online by Cambridge University Press

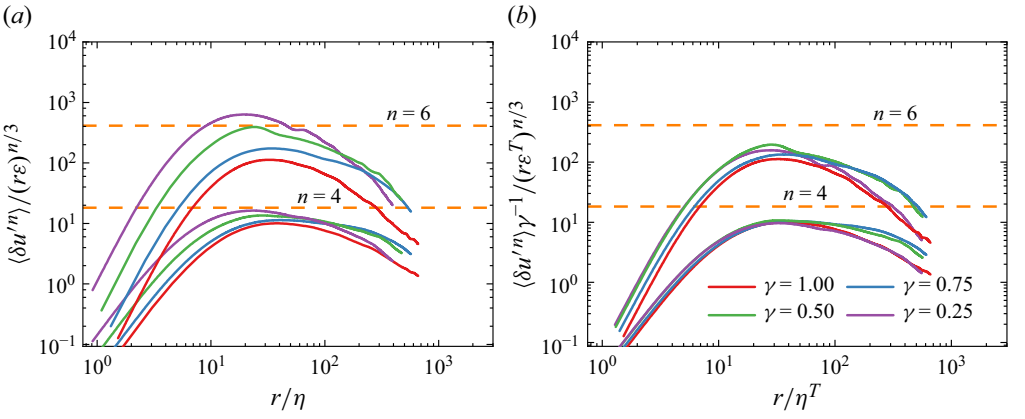


Figure 10. (*a*) Fourth- and sixth-order structure functions and (*b*) the corresponding conditional structure functions at four different cross-wise positions for $Re_H = 10^4$. The horizontal dashed lines indicate the asymptotic values of the Kolmogorov constants C_4^{LSF} and C_6^{LSF} (18.18 and 413.33, respectively) as the Reynolds number approaches infinity. These asymptotic values are determined based on an empirical formula for the structure function (Tang *et al.* 2017).

3.2. *Self-similarity of the conditional higher-order structure functions*

Figure 10 presents the higher even-order (fourth- and sixth-order) structure functions and the corresponding conditional structure functions for $Re_H = 10^4$. The self-similarity of higher-order structure functions differs significantly from that of the second-order structure function discussed already. The profiles of the conditional structure functions exhibit a gradual departure from self-similarity and Kolmogorov's universal equilibrium theory from the jet centre to the edge. Even within the small-scale dissipative range, the conditional fourth- and sixth-order structure functions exhibit clear non-self-similar profiles, with the deviations being more pronounced for the sixth-order case. This finding is consistent with the standard paradigm of higher-order statistics, which are not universal and are highly sensitive to factors such as external intermittency, the FRN effect and intrinsic characteristics of TNTI. A similar observation was also reported in Gauding *et al.* (2021). Moreover, they employed the extended self-similarity (ESS) framework to investigate the relationship between the scaling exponent of the inertia range of the structure function and external intermittency. Their results indicate that the application of the ESS framework does not improve the relative scaling exponent of the inertia range of higher-order structure functions in intermittent regions. Note that the results at the higher Reynolds number $Re_H = 10^5$ are consistent with those at $Re_H = 10^4$. For a higher Reynolds number, the Kolmogorov constants in the fully turbulent region C_4^{LSF} and C_6^{LSF} are closer to their theoretical values at infinite Reynolds number (see figure 11).

Owing to the blocking/sheltering mechanisms of TNTI (Hunt & Durbin 1999; da Silva *et al.* 2014), the turbulence near the TNTI layer can significantly affect the self-similarity of $\langle \delta u'^2 \rangle(r)$ (Xie *et al.* 2025*b*). Their analysis further shows that the conditional second-order structure functions recover self-similarity once the turbulent region within a distance approximately equal to the mean TNTI thickness from its outer edge is excluded. In this study, to eliminate the effect of the TNTI blocking/sheltering mechanism on higher-order structure functions, we computed the conditional structure functions in the high-enstrophy region with $|\boldsymbol{\omega}|_{th} = 0.14\langle|\boldsymbol{\omega}|\rangle_C$, presented in figure 12. Here, the high-vorticity threshold is consistent with the value reported by Xie *et al.* (2025*b*), who found that the average distance between two different iso-surfaces (i.e. $|\boldsymbol{\omega}|_{th} = 0.14\langle|\boldsymbol{\omega}|\rangle_C$ and

https://doi.org/10.1017/jfm.2026.11642 Published online by Cambridge University Press

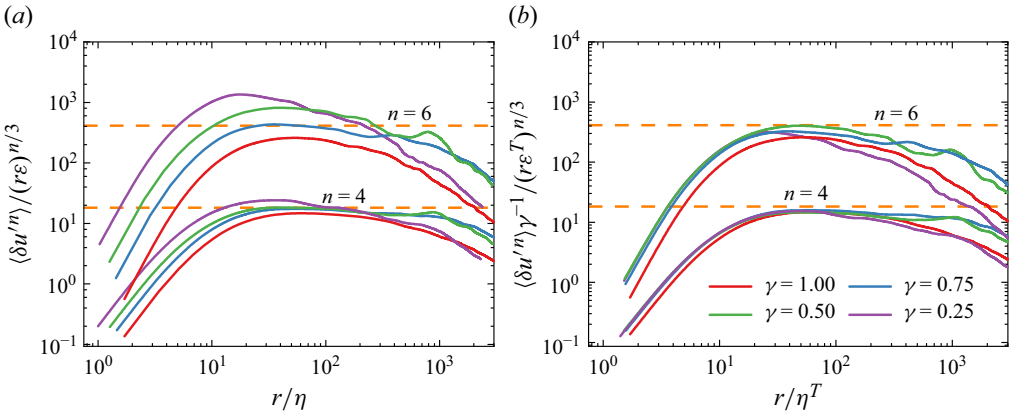


Figure 11. Same as figure 10, but for $Re_H = 10^5$.

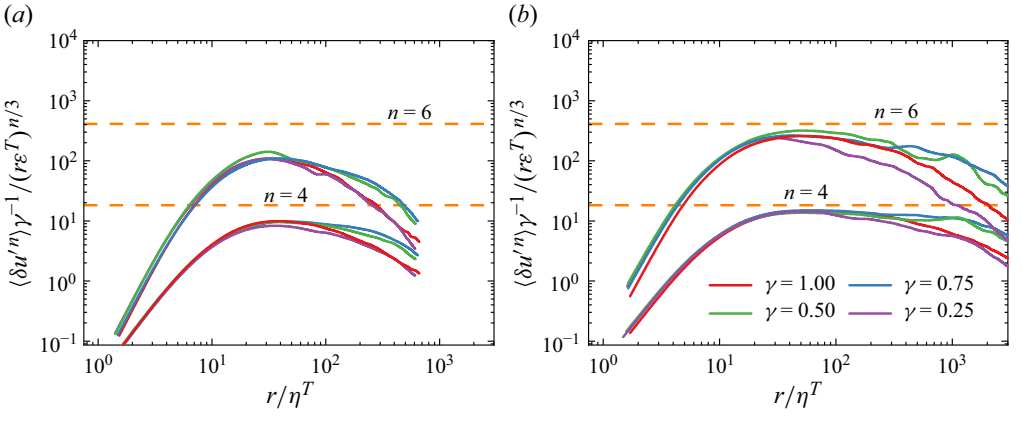


Figure 12. Same as figures 10(*b*) and 11(*b*), but for the vorticity threshold $|\boldsymbol{\omega}|_{th} = 0.14\langle|\boldsymbol{\omega}|\rangle_C$. (*a*) $Re_H = 10^4$; (*b*) $Re_H = 10^5$.

$0.01\langle|\boldsymbol{\omega}|\rangle_C$) is comparable to the mean thickness of the TNTI. Note that the characteristic scales used for normalisation (i.e. ε^T, η^T and γ) are also determined using the modified threshold to mitigate the effects of TNTI. Compared with figures 10(*b*) and 11(*b*), the profiles of the conditional structure functions exhibit a satisfactory collapse at small and intermediate scales in the high-enstrophy region, except for the sixth-order structure function at $Re_H = 10^5$. This may be related to the high sensitivity of higher-order structure functions to the external intermittency. In summary, our findings suggest that the large-scale inhomogeneity and anisotropy near the TNTI significantly affect the behaviour of higher-order structure functions, leading to their deviation from self-similarity.

4. Conditional third-order structure function and contribution of the unsteady term

4.1. *Approach to the Kolmogorov* 4/5 *law in the presence of external intermittency*

The self-similar behaviour of the conditional third-order structure function is further investigated in the context of the self-similar behaviour of the conditional second-order structure function. The third-order structure function, in contrast, is directly related to the energy flux in the inertial range through the Kolmogorov 4/5 law and its distribution

https://doi.org/10.1017/jfm.2026.11642 Published online by Cambridge University Press

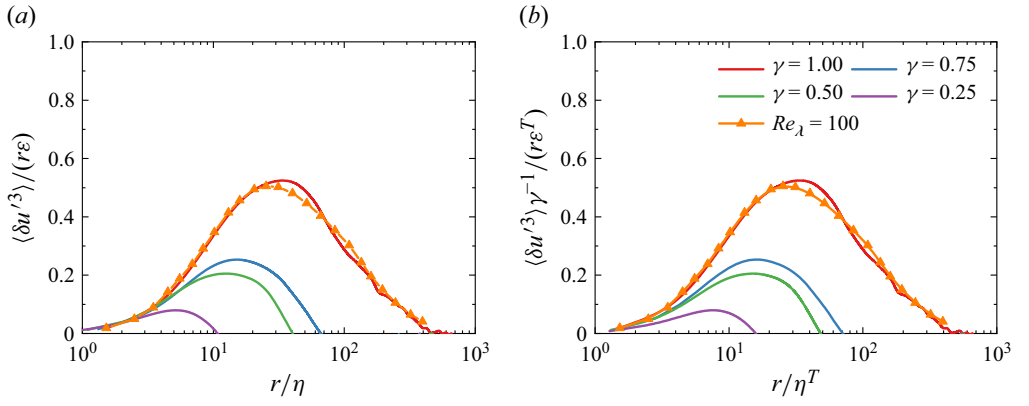


Figure 13. (*a*) Third-order structure function, normalised by the Kolmogorov length scale η and the averaged dissipation rate ε, and (*b*) the corresponding conditional third-order structure function, normalised by the Kolmogorov length scale η^T and the averaged dissipation rate ε^T, of the streamwise velocity fluctuations at four different cross-wise positions for $Re_H = 10^4$. For comparison, the distribution of structure functions is compared with DNS data for grid turbulence with $Re_\lambda = 100$ (Antonia & Burattini 2006).

provides insights into the energy cascade within intermittent regions. The normalised third-order structure functions $-\langle \delta u'^3 \rangle(r)/(r\varepsilon)$ at four different cross-wise positions are plotted (see figures 13*a* and 14*a*). For the lower local Reynolds number $Re_\lambda = 100$, the third-order structure function distribution in the central plane of the jet shows good agreement with DNS results for grid turbulence at Reynolds number $Re_\lambda = 100$ (Antonia & Burattini 2006). It is worth noting that they actually plotted $-\langle \delta u'^3 \rangle(r)/(r\varepsilon)$ versus r/λ, instead of $-\langle \delta u'^3 \rangle(r)/(r\varepsilon)$ versus r/η. According to the local isotropic assumption, the Taylor microscale λ and the Kolmogorov length scale η satisfy $\lambda/\eta = 15^{1/4}(Re_\lambda)^{1/2}$. For a local Reynolds number of $Re_\lambda = 100$, the value of λ/η estimated from this formula is approximately 20. In other words, Antonia & Burattini (2006) actually plotted $-\langle \delta u'^3 \rangle(r)/(r\varepsilon)$ versus $r/(20\eta)$, applying a scaling factor of $SF = 20$. For comparison, after removing the scaling factor SF, the distribution of the structure function collapses together at almost all scales. However, for two different Reynolds numbers, the expected Kolmogorov 4/5 law is not achieved, although it is closer at higher Reynolds numbers (see figure 14*a*).

The maximum values of the structure function $-\langle \delta u'^3 \rangle(r)/(r\varepsilon)$ on the central plane are 0.52 and 0.65, and reveal a significant Reynolds number dependence, as reported by Pearson & Antonia (2001). Recent work by Tang, Antonia & Djenidi (2023) shows that the Reynolds number effect may differ for odd and even orders. Specifically, $-\langle \delta u'^3 \rangle(r)/(r\varepsilon)$ requires a higher Reynolds number than $\langle \delta u'^2 \rangle(r)/(r\varepsilon)^{2/3}$ to establish a discernible inertial range. In the intermittent region, the maximum value $-\langle \delta u'^3 \rangle(r)/(r\varepsilon)$ decreases with decreasing γ (see figure 13*a*). Highly intermittent regions are associated with larger deviations from the Kolmogorov 4/5 law. However, the two-state model analysis in Appendix A suggests that this result cannot be attributed to external intermittency, as it does not affect the Kolmogorov constant in the inertial range for $-\langle \delta u'^3 \rangle(r)$. Instead, one may guess that this is attributed to large-scale motions in the flow. Compared with the fully turbulent region with $\gamma = 1.0$, the intermittent region exhibits significant mean shear, which is expected to affect the behaviour of $-\langle \delta u'^3 \rangle(r)$ in the inertial range.

Figures 13(*b*) and 14(*b*) show the corresponding conditional third-order structure functions for two different Reynolds numbers. For the centre plane of the jet where $\lambda^T/\eta^T = \lambda/\eta$ and $Re_\lambda^T = Re_\lambda$, the DNS result for grid turbulence is also included.

https://doi.org/10.1017/jfm.2026.11642 Published online by Cambridge University Press

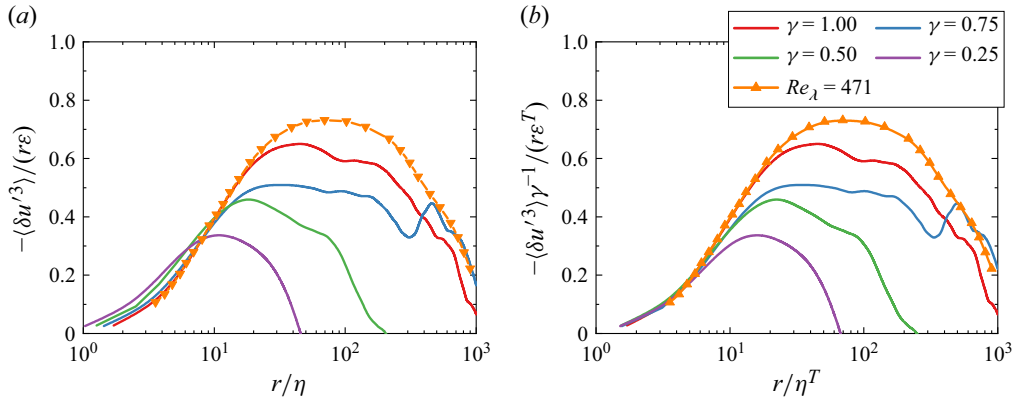


Figure 14. Same as figure 13, but for $Re_H = 10^5$. For comparison, the distribution of structure functions is compared with DNS data for isotropic turbulence with $Re_\lambda = 471$ (Ishihara *et al.* 2009).

The expected self-similarity is not observed at small and intermediate scales. Even for higher Reynolds number, the structure function exhibits self-similarity only at small scales where $r/\eta^T \leqslant 7$. One interesting finding is that the range of self-similarity extends to increasingly larger values of r/η^T at a higher Reynolds number Re_H.

4.2. *Contribution of the unsteady term*

The transport equation for $\langle\delta u'^2\rangle(r)$, i.e. the general form of the Kármán–Howarth equation (Kolmogorov 1941*c*), is used to further investigate the deviation of the third-order structure function from self-similarity at intermediate scales:

$$-\langle\delta u'^3\rangle(r) = \frac{4}{5}r\varepsilon - 6\nu\frac{\partial}{\partial r}\langle\delta u'^2\rangle(r) - I_u(r), \tag{4.1}$$

where the second term on the right-hand side denotes the viscous term. The last term represents the unsteady term $I_u(r)$, which reflects the effect of large-scale motion on the structure function (Danaila *et al.* 1999; Hill 2001; Kaneda, Yoshino & Ishihara 2008). For the temporally evolving plane jet, $I_u(r)$ can be expressed as (Danaila *et al.* 2001; Kaneda *et al.* 2008)

$$I_u(r) = -\frac{3}{r^4}\int_0^r s^4\left[\frac{\partial\langle\delta u'^2\rangle(s)}{\partial t}\right]\mathrm{d}s - \frac{6}{r^4}\int_0^r s^4\left[\frac{\partial\langle\delta v'\delta u'^2\rangle(s)}{\partial Y}\right]\mathrm{d}s, \tag{4.2}$$

where s is a dummy variable. A detailed description of the self-similarity analysis of the third-order structure function is provided in Appendix C. Note that the self-similarity analysis based on the Kármán–Howarth equation neglects the contribution of $I_u(r)$, since this term can be considered negligible in the inertial range under the assumption of infinite Reynolds number. However, for the current finite Reynolds number case, the unsteady term is expected to have a significant effect on $-\langle\delta u'^3\rangle(r)/(r\varepsilon^T)$ (Antonia & Burattini 2006; Tang *et al.* 2023), especially in the intermittent region. Therefore, it is important to consider the contribution of the unsteady term, as shall be discussed later.

After dividing (4.1) by $r\varepsilon$, the normalised form of the equation is given by

$$-T_r^* = 4/5 - V_r^* - I_u^*(r), \tag{4.3}$$

where the superscript $*$ represents the normalised variable. In particular, (4.3) can be written as $-T_{\lambda^T}^* = 4/5 - V_{\lambda^T}^* - I_u^*(\lambda^T)$ when $r = \lambda^T$. It should be noted that $r = \lambda^T$

https://doi.org/10.1017/jfm.2026.11642 Published online by Cambridge University Press

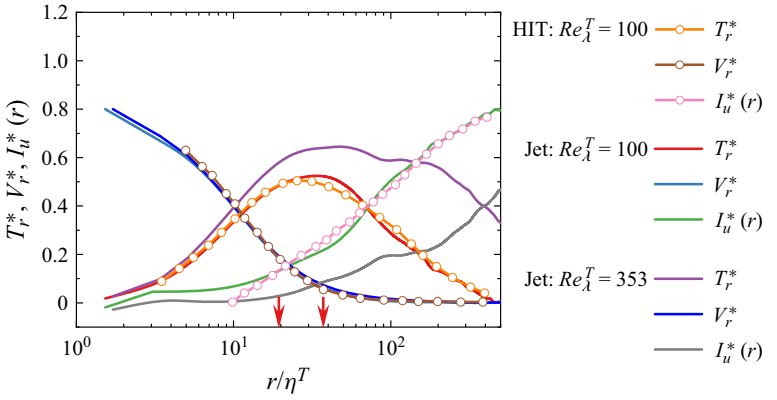


Figure 15. Variation of each term in the generalised transport equation with respect to the separation distance r on the central plane of the jet at two different Reynolds numbers. Only the scale range where the deviation from local isotropy is less than 20 % is shown. The left and right vertical arrows indicate the positions of $r = \lambda^T$ at $Re_\lambda^T = 100$ and 353, respectively. For comparison, each term of the transport equation is compared with DNS data from decaying grid turbulence at the same Taylor Reynolds number of $Re_\lambda^T = 100$ (Antonia & Burattini 2006). Note that each term in the transport equation from the results of Antonia & Burattini (2006) has been rescaled by removing the scaling factor $SF = 20$, which is determined from the relation $\lambda^T/\eta^T = 15^{1/4}(Re_\lambda^T)^{1/2}$.

represents a scale located near the lower end of the inertial range. Tang *et al.* (2017) have investigated the effect of $I_u^*(\lambda^T)$ on the Kolmogorov 4/5 law in different flow types (e.g. grid turbulence, circular and square cylinder wakes, jet axis and channel centreline, etc.). These studies show that $I_u^*(\lambda^T)$ can significantly influence the behaviour of scales within the inertial range. To date, the influence of the dynamical characteristics of the unsteady term $I_u^*(\lambda^T)$ on the third-order structure function in the intermittent region still remains elusive.

Considering the significant effect of the Reynolds number on the third-order structure function $-\langle \delta u'^3 \rangle(r)$ (see figures 13 and 14), the contribution of the unsteady term $I_u^*(r)$ is evaluated at three different cross-wise positions with $\gamma = 1.0$, 0.75 and 0.5. Each term of the generalised transport equation on the jet central plane at two different Reynolds numbers is plotted in figure 15. Note that only the scale range where the deviation from local isotropy is less than 20 % is shown, i.e. $r/\eta^T < 500$ (see figure 23). Each term of the equation in the fully turbulent region shows reasonably good agreement with DNS results for grid turbulence at a similar Taylor Reynolds number $Re_\lambda^T = 100$ across almost all scales (Antonia & Burattini 2006). This suggests that the scale-by-scale energy budget may exhibit similar statistical characteristics even for different types of turbulent flows. Tang *et al.* (2017) found that the value of $I_u^*(\lambda^T)$ at $r = \lambda^T$ varies significantly across different flows. Specifically, $I_u^*(\lambda^T)$ is smallest in stationary forced periodic box turbulence and largest along the centreline of the channel flow. With increasing Re_λ^T, the unsteady term $I_u^*(r)$ gradually decreases, while the third-order structure function T_r^* gradually increases. In contrast, the viscous term V_r^* appears to be independent of the local Reynolds number Re_λ^T. The unsteady term $I_u^*(r)$ is negligible when $r/\eta^T < 8$, indicating that large-scale motions have little effect on small-scale motions, as reported by Danaila *et al.* (1999).

The examination of local isotropy at each scale is provided in Appendix C. The local isotropy approximately satisfied at $r = \lambda^T$ enables us to make a rough estimate of the contribution of $I_u(r)$ in the intermittent region at the same scale. Table 3 lists the values of each term $T_{\lambda^T}^*$, $V_{\lambda^T}^*$ and $I_u^*(\lambda^T)$ in the transport equation at $r = \lambda^T$ for three different

https://doi.org/10.1017/jfm.2026.11642 Published online by Cambridge University Press

Re_H	γ	Re_λ^T	$T^*_{\lambda^T}$	$V^*_{\lambda^T}$	$I^*_u(\lambda^T)$	Re_H	γ	Re_λ^T	$T^*_{\lambda^T}$	$V^*_{\lambda^T}$	$I^*_u(\lambda^T)$
	1.0	100	0.476	0.197	0.127	—	1.0	353	0.646	0.073	0.081
10^4	0.75	136	0.240	0.141	0.419	10^5	0.75	527	0.507	0.050	0.243
	0.5	114	0.197	0.153	0.450	—	0.5	459	0.401	0.055	0.344

Table 3. Values of each term $T^*_{\lambda^T}$, $V^*_{\lambda^T}$ and $I^*_u(\lambda^T)$ in the transport equation at $r=\lambda^T$ for there different cross-wise positions with $\gamma=1.0$, 0.75 and 0.5 at two different Reynolds numbers ($Re_H=10^4$ and 10^5). The conditional local Reynolds numbers Re_λ^T at two cross-wise positions are also listed.

cross-wise positions with $\gamma=1.0$, 0.75 and 0.5 at two Reynolds numbers ($Re_H=10^4$ and 10^5). As expected, the contribution of the unsteady term $I^*_u(\lambda^T)$ in the intermittent region is larger than that in the jet central plane at a fixed separation distance $r=\lambda^T$. According to § 3.1, the conditional longitudinal second-order structure function exhibits self-similarity at small and intermediate scales, indicating that the viscous term V^*_r also exhibits self-similarity over these scales. For two different cross-wise positions (i.e. $\gamma=1.0$ and 0.5) of $Re_H=10^4$, it is also worth noting that the two positions have approximately the same conditional local Reynolds number Re_λ^T. This indicates that the significant deviation of $T^*_{\lambda^T}$ at two different cross-wise positions is unlikely to be caused by Reynolds number effects. Instead, this deviation is attributed to the contribution of $I^*_u(\lambda^T)$. For the lower Reynolds number, the values of $I^*_u(\lambda^T)$ at $\gamma=1.0$ and 0.5 are 0.127 and 0.450, respectively, while for the higher Reynolds number, the values at the same positions are 0.081 and 0.344. This means that the contribution of $I^*_u(\lambda^T)$ decreases as Re_λ^T increases and increases as γ decreases. In summary, the larger contribution of $I^*_u(\lambda^T)$ at $\gamma=0.5$ compared with that at $\gamma=1.0$ indicates that large-scale motions are responsible for the significant deviation from self-similarity of the third-order structure function within the inertial range (see figures 13*b* and 14*b*). Nevertheless, as the local Reynolds number increases, the contribution of $I^*_u(r)$ in the inertial range gradually decreases and, thus, the self-similar behaviour of the third-order structure function is expected to be recovered at sufficiently high Reynolds numbers.

5. Finite-Reynolds-number effects of structure function

5.1. *Comparison between the empirical prediction and numerical data at $\gamma=1.0$*

To further investigate the FRN effect of the structure functions, an empirical formula for $\langle \delta u'^n \rangle(r)$ is used to indirectly estimate the behaviour of the structure function at high Reynolds numbers (Dhruva 2000; Kurien & Sreenivasan 2000), that is,

$$\frac{\langle \delta u'^n \rangle\left(r/\eta^T\right)}{\left(v_\eta^T\right)^n} = \frac{1}{15^{n/2}} F_n \frac{\left(r/\eta^T\right)^n \left(1+D_n r/L^T\right)^{2C_n-n}}{\left(1+B_n(r/\eta^T)^2\right)^{C_n}}, \tag{5.1}$$

where B_n, C_n, D_n and F_n ($=\langle(\partial u'/\partial x)^n\rangle/\langle(\partial u'/\partial x)^2\rangle^{n/2}$) are constants that satisfy the asymptotic case for infinite Reynolds number. Following Antonia & Burattini (2006) and Tang *et al.* (2023), the values of the empirical parameters B_n and D_n are determined by trial and error until (5.1) fits the data of $\langle \delta u'^n \rangle(r/\eta^T)$ at two different Re_λ^T. In particular, substituting the isotropic relations ($L^T/\eta^T = C_\varepsilon^T 15^{-3/4}(Re_\lambda^T)^{3/2}$ and $(u^T_{rms})^2/(v_\eta^T)^2 = Re_\lambda^T/15^{1/2}$) into (5.1) yields $C_n=n/3$, since the prefactor of the structure function is independent of the Reynolds number. Here, C_ε^T and u^T_{rms} are

https://doi.org/10.1017/jfm.2026.11642 Published online by Cambridge University Press

the conditional non-dimensional dissipation rate and r.m.s. of the conditional velocity fluctuations, respectively. Clearly, the term $D_n r/L^T$ is associated with the large-scale motions of the flow, which involves the conditional integral length scale L^T, as well as the constraint constant D_n. However, for the intermittent region with $\gamma = 0.5$, L^T cannot be directly determined from the velocity auto-correlation function due to the interference of laminar signals in the intermittent regions. As a result, the conditional non-dimensional dissipation rate $C_\varepsilon^T = L^T \varepsilon^T/(u'^T)^3$ cannot be calculated directly. Following the approach of Gauding *et al.* (2021) for defining conditional structure functions in the intermittent region, we define the conditional velocity auto-correlation function $f_u^{TT}(\boldsymbol{x}, r)$ in a similar manner, i.e.

$$f_u^{TT}(\boldsymbol{x}, r) = \frac{\langle H(\boldsymbol{x}) H(\boldsymbol{x} + r\boldsymbol{e}_1) u'(\boldsymbol{x}) u'(\boldsymbol{x} + r\boldsymbol{e}_1)\rangle}{\langle (u'^T)^2(x)\rangle}. \tag{5.2}$$

The formula defines an intermittent function $H(X, Y, Z)$ to mark the flow state of the fluid to describe the intermittency of the flow, where $|\boldsymbol{\omega}| \geq |\boldsymbol{\omega}|_{th}$ is marked as 1 to indicate the turbulent region and $|\boldsymbol{\omega}| < |\boldsymbol{\omega}|_{th}$ is marked as 0 to indicate the laminar region. The advantage of this formula is that it ensures the state of the two locations ($u'(\boldsymbol{x} + r\boldsymbol{e}_1)$ and $u'(\boldsymbol{x})$) is restricted to the turbulent portion of the jet. It is worth noting that the jet centre plane lies in a fully turbulent region, where the intermittent function $H(X, Y, Z)$ is always equal to 1. Consequently, the conditional velocity auto-correlation function is identical to the normal velocity auto-correlation function. In contrast, for the intermittent region with $\gamma = 0.5$, the conditional velocity auto-correlation function can exclude influences of the laminar motions on the conditional integral length scale L^T. Based on (5.2), L^T can be directly obtained by integrating the conditional velocity auto-correlation function $f_u^{TT}(\boldsymbol{x}, r)$ and the conditional non-dimensional dissipation rate is evaluated by $C_\varepsilon^T = L^T \varepsilon^T/(u'^T)^3$. Numerical integration of $f_u^{TT}(\boldsymbol{x}, r)$ shows that the integral length scale L^T in the jet centre plane is approximately $112\eta^T$, corresponding to the conditional non-dimensional dissipation rate $C_\varepsilon^T = 0.86$. For the intermittent region with $\gamma = 0.5$, L^T is approximately $144\eta^T$ and the corresponding conditional non-dimensional dissipation rate is $C_\varepsilon^T = 0.92$. As expected, the values of the conditional non-dimensional dissipation rate are approximately the same. The slight differences may be related to the intrinsic characteristics of TNTI. Watanabe *et al.* (2019*a*) investigated the non-dimensional dissipation rate C_ε near the TNTI. The results indicate that C_ε is significantly higher in the TNTI sublayer (i.e. the turbulent sublayer) than in the turbulent core region.

According to the local isotropic assumption, the relationship between $\langle \delta u'^2 \rangle$ and $\langle \delta v'^2 \rangle$ satisfies (C1). For $n = 2$, combining with (5.1) and (C1), a good approximation for $\langle \delta v'^2 \rangle(r)$ can be written as

$$\left\langle \delta v'^2 \right\rangle = \frac{F_2 (r/\eta)^2 (1 + D_2 r/L)^{(2C_2 - 2)}}{15(1 + B_2 (r/\eta)^2)^{C_2}} \left(2 + \frac{(2C_2 - 2) D_2 r/L}{2(1 + D_2 r/L)} - \frac{C_2 B_2 (r/\eta)^2}{1 + B_2 (r/\eta)^2} \right). \tag{5.3}$$

It should be emphasised that the parameters B_n and D_n can be adjusted in different regions since (5.1) is mainly used to effectively fit the measured data of $\langle \delta u'^n \rangle(r)$ in a specific flow region (Antonia *et al.* 2019*b*). This approach enables us to extrapolate the existing results to the Reynolds number range that cannot be directly obtained by experiments or numerical simulations. Dhruva (2000) conducted detailed tests on the empirical formula and the results showed that the formula provides a good agreement with atmospheric surface layer data across the entire range of r. Antonia & Burattini (2006) investigated the FRN effect on third-order structure functions in forced and decaying turbulence based on empirical formula.

https://doi.org/10.1017/jfm.2026.11642 Published online by Cambridge University Press

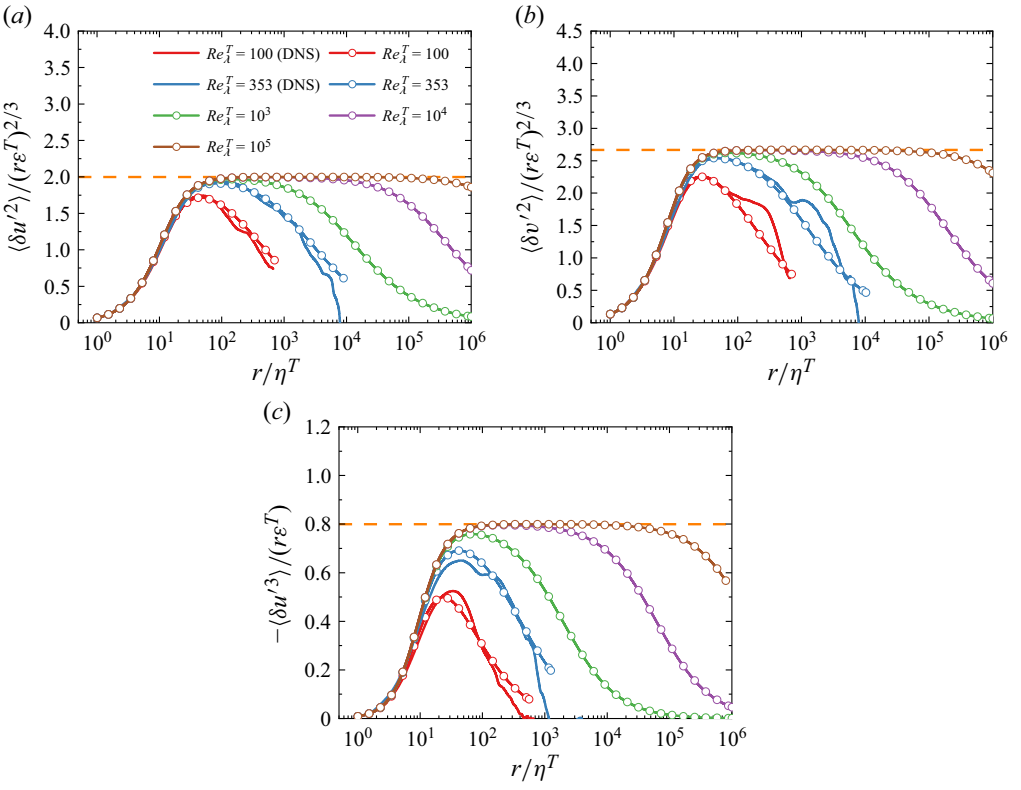


Figure 16. Distributions of structure functions in the fully turbulent region with $\gamma = 1.0$, based on (5.1), at $Re_\lambda^T = 100$, 353, 10^3, 10^4 and 10^5. (*a*) $\langle \delta u'^2 \rangle(r)/(r\varepsilon^T)^{2/3}$; (*b*) $\langle \delta v'^2 \rangle(r)/(r\varepsilon^T)^{2/3}$; (*c*) $-\langle \delta u'^3 \rangle(r)/(r\varepsilon^T)$. The solid lines of the same colour represent the corresponding DNS results for the turbulent plane jet. The horizontal dashed line shows the asymptotic value of the Kolmogorov constant as the Reynolds number approaches infinity.

Figure 16 presents a comparison between the numerical results of the structure function and the empirical formula in the jet centre plane. The parameters C_ε, B_n, C_n, D_n and F_n used to fit the structure functions are summarised in table 4. Here, the values of B_2, C_2, D_2 and F_2 differ slightly from the grid turbulence data reported by Tang *et al.* (2023). In their study, $B_2 = 0.0056$ was used, whereas we used $B_2 = 0.006$ to achieve a better fit to the data; this value is consistent with that reported by Antonia *et al.* (2019*b*). The numerical results show reasonably good agreement with the empirical formula at the small and intermediate scales for two different local Reynolds numbers Re_λ^T. This confirms that the empirical formula effectively describes the available data for $\langle \delta u'^2 \rangle(r)$, $\langle \delta v'^2 \rangle(r)$ and $-\langle \delta u'^3 \rangle(r)$. The good agreement makes it possible to extrapolate the existing results to higher local Reynolds numbers Re_λ^T. It should be pointed out that the agreement between the model and data at large scales is poor, which is likely due to the difficulty of achieving statistical convergence at those scales. Specifically, the distribution of $\langle \delta v'^2 \rangle(r)$ at $Re_\lambda^T = 353$ exhibits an unexpected oscillation at approximately $r/\eta = 1500$. Although we performed repeated simulations to mitigate this issue as much as possible, the available data gradually decreases with increasing r, possibly leading to the emergence of an unexpected oscillation.

https://doi.org/10.1017/jfm.2026.11642 Published online by Cambridge University Press

C_ε	B_2^u	C_2^u	D_2^u	F_2^u	B_2^v	C_2^v	D_2^v	F_2^v	B_3^u	C_3^u	D_3^u	F_3^u
0.86	0.006	0.667	1.09	1.0	0.006	0.667	0.553	1.0	0.0114	1.0	1.84	0.53

Table 4. Values of parameters B_n, C_n, D_n and F_n in (5.1) within the jet centre plane. Note that the superscripts u and v denote the fitting parameters for the longitudinal and transverse structure functions, respectively.

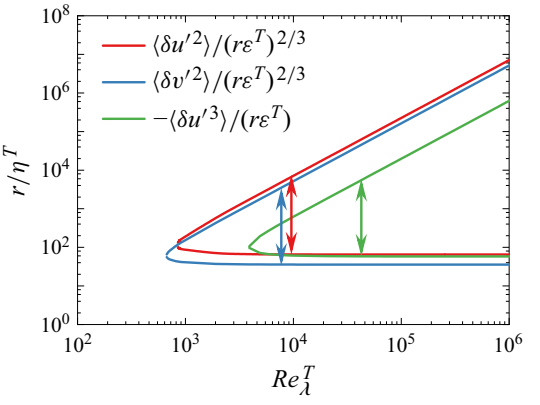


Figure 17. Range of normalised separation distance r/η^T in the jet centre plane over which the empirical distributions of $\langle\delta u'^2\rangle$, $\langle\delta v'^2\rangle$ and $-\langle\delta u'^3\rangle$ deviate from 2.00, 2.66 and 0.798, respectively, by less than 2.5 %. The separation distance between the curves approximately represents the upper and lower limits of the inertial range at a fixed conditional local Reynolds number Re_λ^T. The vertical arrows indicate the approximate values of Re_λ required to achieve an inertial range of two decades in extent for $\langle\delta u'^2\rangle(r)/(r\varepsilon^T)^{2/3}$ (red arrow), $\langle\delta v'^2\rangle(r)/(r\varepsilon^T)^{2/3}$ (blue arrow) and $-\langle\delta u'^3\rangle(r)/(r\varepsilon^T)$ (green arrow).

The extrapolated results in figure 16 also show that when Re_λ^T tends to infinity, the Kolmogorov constants for $\langle\delta u'^2\rangle(r)$, $\langle\delta v'^2\rangle(r)$ and $-\langle\delta u'^3\rangle(r)$ are 2.00, 2.676 and 0.798, respectively, which are consistent with the theoretically predicted values. For $Re_\lambda^T = 10^4$, the distribution of $\langle\delta u'^2\rangle(r)$ exhibits a discernible plateau over more than one decade in extent, whereas a similar discernible plateau in the distribution of $-\langle\delta u'^3\rangle(r)$ is only observed at $Re_\lambda^T = 10^5$. This suggests that FRN effects may differ between the second- and third-order structure functions. To satisfy the K41 theoretical prediction, i.e. $\langle\delta u'^n\rangle(r) \sim r^{n/3}$, the third-order structure function may require a much higher Re_λ^T.

The approximate value of Re_λ^T required to establish the inertial range for the structure functions $\langle\delta u'^n\rangle(r)$ is estimated from the range of normalised separation distances r/η^T in the jet centre plane. As shown in figure 17, this range corresponds to where the normalised structure functions $\langle\delta u'^2\rangle(r)/(r\varepsilon^T)^{2/3}$, $\langle\delta v'^2\rangle(r)/(r\varepsilon^T)^{2/3}$ and $-\langle\delta u'^3\rangle(r)/(r\varepsilon^T)$ deviate from their theoretical predictions by less than 2.5 %. The vertical arrows indicate the approximate values of Re_λ^T required to achieve an inertial range of two decades in extent. The corresponding Reynolds numbers Re_λ^T for $\langle\delta u'^2\rangle(r)/(r\varepsilon^T)^{2/3}$, $\langle\delta v'^2\rangle(r)/(r\varepsilon^T)^{2/3}$ and $-\langle\delta u'^3\rangle(r)/(r\varepsilon^T)$ are approximately 9×10^3, 8×10^3 and 4×10^4, respectively. As Re_λ^T increases, the inertial range continues to expand. This observation somewhat echoes the argument by Antonia *et al.* (2019*b*) that FRN effects should be properly considered before determining whether modifications to K41 are necessary.

https://doi.org/10.1017/jfm.2026.11642 Published online by Cambridge University Press

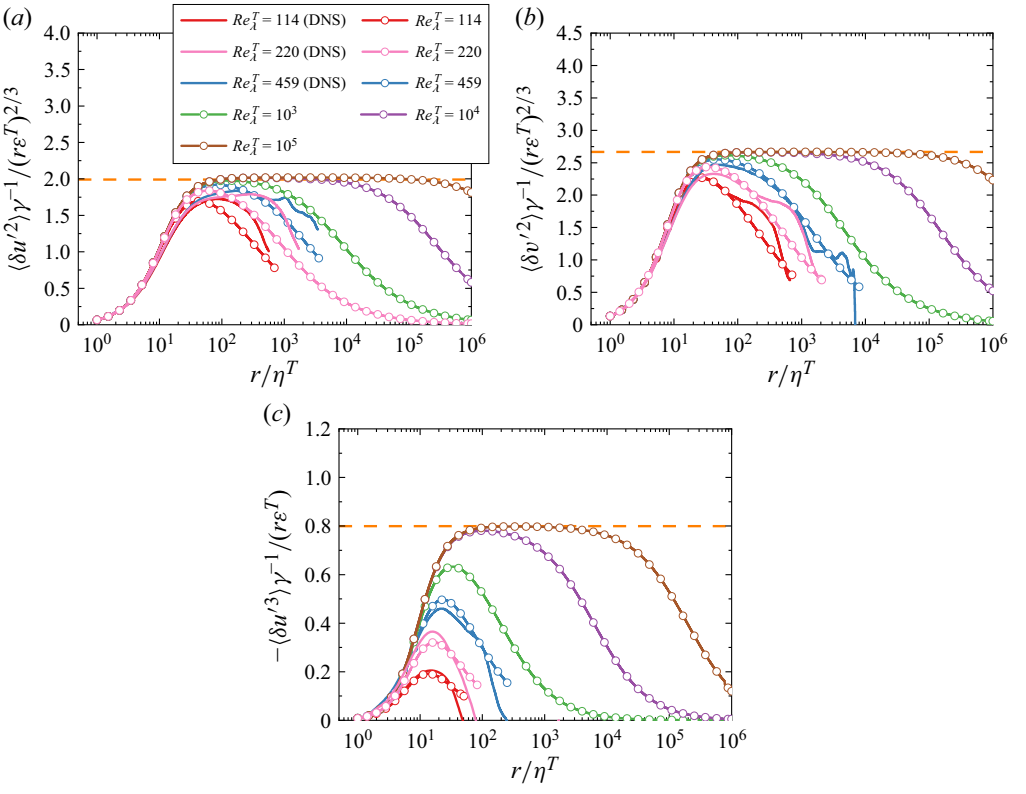


Figure 18. Distributions of conditional structure functions in the intermittent region with $\gamma = 0.5$, based on (5.1), at $Re_\lambda^T = 114$, 220, 459, 10^3, 10^4 and 10^5. (*a*) $\langle \delta u'^2 \rangle(r)/(r\varepsilon^T)^{2/3}$; (*b*) $\langle \delta v'^2 \rangle(r)/(r\varepsilon^T)^{2/3}$; (*c*) $-\langle \delta u'^3 \rangle(r)/(r\varepsilon^T)$. The solid lines of the same colour represent the corresponding DNS results for the turbulent plane jet. Noted that the distribution of the structure functions for the global Reynolds number $Re_H = 4 \times 10^4$ is plotted, with the data taken from Watanabe *et al.* (2019*b*).

5.2. *Finite Reynolds number effect on structure functions in the intermittent region*

A comparison between the numerical results of the conditional structure function and the empirical formula at $\gamma = 0.5$ is presented in figure 18. The corresponding parameters C_ε, B_n, C_n, D_n and F_n used to fit the structure functions are summarised in table 5. For the conditional second-order structure function, although large-scale fluctuations are not universal, the differences between the curves of the conditional second-order structure functions at large scales are not pronounced (see figures 5*b*, 6*b*, 7*b* and 8*b*). Therefore, the constant D_2 requires only slight adjustments. Conversely, for the conditional third-order structure function, significant differences are observed at large scales (see figures 13*b* and 14*b*). This means that the term $D_3 r/L^T$, related to large-scale fluctuations, needs to be adjusted to accurately fit the behaviour of the structure function at large scales. Therefore, the value of the constant D_3 differs considerably between $\gamma = 1$ and $\gamma = 0.5$. To enhance the reliability of the statistical results, the structure function profiles of the temporally evolving plane jet for the global Reynolds number $Re_H = 4 \times 10^4$ from Watanabe *et al.* (2019*b*) are also shown. The corresponding conditional local Reynolds number Re_λ^T is approximately 220 at $\gamma = 0.5$. Except for the conditional longitudinal structure function $\langle \delta u'^2 \rangle(r)\gamma^{-1}/(r\varepsilon^T)^{2/3}$, the numerical results collapse reasonably well with the empirical formula at small and intermediate scales. This means that the empirical formula (5.1)

https://doi.org/10.1017/jfm.2026.11642 Published online by Cambridge University Press

C_ε	B_2^u	C_2^u	D_2^u	F_2^u	B_2^v	C_2^v	D_2^v	F_2^v	B_3^u	C_3^u	D_3^u	F_3^u
0.92	0.006	0.667	0.94	1.0	0.006	0.667	0.836	1.0	0.0114	1.0	19.7	0.53

Table 5. Same as table 4, but for $\gamma = 0.5$.

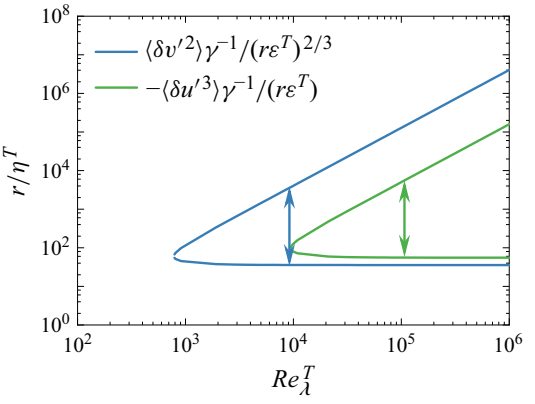


Figure 19. Same as figure 17, but for $\gamma = 0.5$. Note that the extrapolation results of the conditional longitudinal structure function are not shown, since (5.1) fails to adequately describe its behaviour.

seems to be difficult to describe the behaviour of $\langle\delta u'^2\rangle(r)\gamma^{-1}/(r\varepsilon^T)^{2/3}$ in the intermittent region. This deviation may result from the influence of the intrinsic characteristics of the TNTI on the inertial range of the longitudinal structure functions (see figure 12). The extrapolation results in figures 18(*b*) and 18(*c*) indicate that the conditional structure functions $\langle\delta v'^2\rangle(r)\gamma^{-1}/(r\varepsilon^T)^{2/3}$ and $-\langle\delta u'^3\rangle(r)\gamma^{-1}/(r\varepsilon^T)$ may satisfy the classical K41 theory predictions even in the highly inhomogeneous intermittent region when Re_λ^T is sufficiently large.

According to § 3, due to the effect of external intermittency, the Kolmogorov constant C_2^{TSF} for $\langle\delta v'^2\rangle(r)$ exhibits a power-law dependence on the intermittency factor γ, i.e. $C_2^{TSF} \sim \gamma^{1/3}$, while the Kolmogorov constant C_3^{LSF} is unaffected by the external intermittency (see Appendix A). This means that the Kolmogorov constant C_3^{LSF} in the intermittent region may approach 4/5 at infinite Reynolds number, as shown in figure 18(*c*). These results clearly reflect FRN effects on the structure functions.

Figure 19 presents the range of normalised separation distances r/η^T at $\gamma = 0.5$ over which $\langle\delta v'^2\rangle(r)\gamma^{-1}/(r\varepsilon^T)^{2/3}$ and $-\langle\delta u'^3\rangle(r)\gamma^{-1}/(r\varepsilon^T)$ depart from 2.66 and 0.798, respectively, by no more than 2.5 %. Note that the extrapolation results of the conditional longitudinal structure function are not shown here, since (5.1) fails to adequately describe its behaviour (see figure 18*a*). The vertical arrows indicate the approximate values of Re_λ^T required to achieve an inertial range of two decades in extent. For $\langle\delta v'^2\rangle(r)\gamma^{-1}/(r\varepsilon^T)^{2/3}$ and $-\langle\delta u'^3\rangle(r)\gamma^{-1}/(r\varepsilon^T)$, the values of Re_λ^T corresponding to the positions of the arrows need to reach approximately 10^4 and 10^5, respectively. Compared with figure 17, the values of Re_λ^T required in the intermittent region with $\gamma = 0.5$ are significantly higher than those obtained in the jet centre plane. This is expected since the contribution of unsteady terms $I_u^*(\lambda^T)$ is greater in the intermittent region than in the jet centre plane.

It is helpful to examine the self-similarity of the third-order structure function using (5.1) at high local Reynolds numbers. Figure 20 shows the variation of the conditional

https://doi.org/10.1017/jfm.2026.11642 Published online by Cambridge University Press

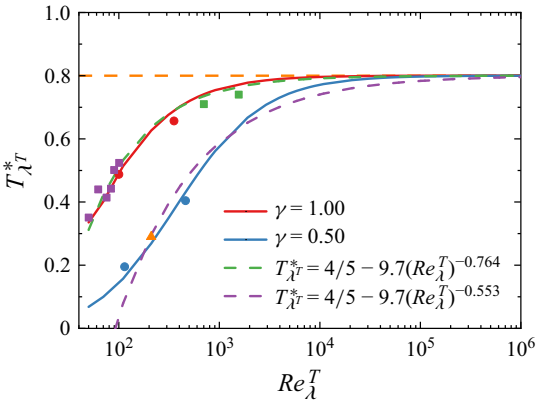


Figure 20. Variation of $T^*_{\lambda^T}$ with Re^T_λ at two different cross-wise positions with $\gamma = 0.5$ and 1.0, based on (5.1). The horizontal dashed line indicates $T^*_{\lambda^T} = 0.8$. The red (●) and blue (●) solid circles correspond to the data at the two different Reynolds numbers considered in the present study. Purple (■) and green (■) squares correspond to the grid turbulence data from Zhou & Antonia (2000) and Tang *et al.* (2023), respectively. The orange triangle (▲) corresponds to the data from the intermittent region with $\gamma = 0.5$ in the temporally evolving turbulent plane jet at $Re_H = 4 \times 10^4$ (Watanabe *et al.* 2019*b*).

third-order structure function $T^*_{\lambda^T}$ with Re^T_λ at $r = \lambda^T$ for $\gamma = 1.0$ and 0.5, based on (5.1). The conditional Taylor microscale λ^T is determined based on the assumption of local isotropy (i.e. $\lambda^T/\eta^T = 15^{1/4}(Re^T_\lambda)^{1/2}$), since the turbulence in the intermittent region also satisfies local isotropy at small scales (see figure 23 in Appendix C). For the fully turbulent region with $\gamma = 1.0$, the extrapolated results are compared with data obtained by Zhou & Antonia (2000) and Tang *et al.* (2023) in grid turbulence. It can be observed that the results from grid turbulence show a good agreement with the extrapolated results. There seem to be no earlier works on the conditional third-order structure function for the intermittent region with $\gamma = 0.5$. We have supplemented an additional DNS result from Watanabe *et al.* (2019*b*). Nevertheless, a good agreement can still be observed. For two different cross-wise positions, the contribution of the unsteady term at $r = \lambda^T$ becomes negligible only when the local Reynolds number reaches approximately 10^4 and 10^5, respectively. This means that when Re^T_λ is greater than 10^5, the conditional third-order structure functions at different positions are expected to recover self-similarity in the range of $r < \lambda^T$. Correspondingly, a higher local Reynolds number is required for the conditional third-order structure function to exhibit self-similarity at small and intermediate scales. It should be noted that the maximum local Reynolds number Re^T_λ achieved in the current experimental measurements is approximately 5000 (Tabeling *et al.* 1996; Belin *et al.* 1997), whereas the maximum Re^T_λ obtained in DNS is much smaller, approximately 2500 (Yeung *et al.* 2025). The value of $Re^T_\lambda = 10^5$ is far beyond the local Reynolds number range currently achievable through experiments or numerical simulations.

A simple algebraic model is used to quantify, albeit approximately, the dependence of $T^*_{\lambda^T}$ on Re^T_λ at $r = \lambda^T$. We use the following expression for $T^*_{\lambda^T}$ as a function of Re^T_λ, namely, $T^*_{\lambda^T} = 4/5 - C(Re^T_\lambda)^D$, where C and D are constants determined by nonlinear least squares fitting. The numerical results show reasonably good agreement with the empirical formula indicating that the empirical parameters are independent of Re^T_λ at a fixed cross-wise position. For the positions where $\gamma = 1.0$ and 0.5, the expression for $T^*_{\lambda^T}$

https://doi.org/10.1017/jfm.2026.11642 Published online by Cambridge University Press

is given by

$$T^*_{\lambda^T} = \frac{4}{5} - 9.7\left(Re^T_\lambda\right)^{-0.764} \quad \text{and} \quad T^*_{\lambda^T} = \frac{4}{5} - 9.7\left(Re^T_\lambda\right)^{-0.553}. \tag{5.4}$$

As shown in figure 20, the selected constant C and D fit the data reasonably well for the fully turbulent region with $\gamma = 1.0$. For the intermittent regions with $\gamma = 0.5$, the simplified curve deviates moderately from (5.1) and the three data points, particularly in the range $Re^T_\lambda < 350$. This deviation may be attributed to the blocking/sheltering mechanisms of TNTI (da Silva *et al.* 2014). The turbulence near the TNTI layer is characterised by large-scale inhomogeneity and anisotropy at low Reynolds numbers (Zhang *et al.* 2023), which implies that the simplified equation cannot adequately capture the characteristics of the third-order structure function within the intermittent region. In contrast, at higher Reynolds numbers, the deviation is small with a maximum error of less than 10 % relative to (5.1). Note that the smaller value of $T^*_{\lambda^T}$ in the intermittent region at $\gamma = 0.5$ is primarily due to a larger contribution from the unsteady term at $r = \lambda^T$ compared with the fully turbulent region (see table 3). Therefore, a smaller intermittent factor γ corresponds to a larger constant D, which stems from the larger unsteady term $I_u(\lambda^T)$ in the intermittent region. To our knowledge, this should be the first time reasonable evidence has supported the possibility that the conditional structure functions in the intermittent region may satisfy K41 predictions.

6. Conclusion

A deeper understanding of the behaviour of structure functions in intermittent regions is crucial for modelling intermittent flows. Currently, the self-similarity of structure functions and the FRN effect on structure functions in the intermittent region are not yet fully understood. The behaviour of structure functions at different cross-wise positions was investigated using DNS of temporally evolving turbulent plane jets at $Re_H = 10^4$ and 10^5 with state-of-the-art massively parallel computations.

For the higher Reynolds number case of $Re_H = 10^5$, the conditional longitudinal and transverse second-order structure functions exhibit self-similar behaviour at the small and intermediate scales when normalised by the conditional Kolmogorov scales. Compared with $Re_H = 10^4$, the deviation from self-similarity of the conditional second-order structure function is not observed at $\gamma = 0.25$ for $Re_H = 10^5$. This behaviour may be related to the fact that the influence of the TNTI becomes less significant, the turbulence near the TNTI layer tending to become more isotropic at higher Reynolds numbers. The self-similarity of the structure function implies that the Kolmogorov constants C_2^{LSF} and C_2^{TSF} for $\langle \delta u'^2 \rangle(r)$ and $\langle \delta v'^2 \rangle(r)$ exhibit a power-law dependence on the intermittency factor γ, i.e. $C_2^{LSF} \sim \gamma^{1/3}$ and $C_2^{TSF} \sim \gamma^{1/3}$. The scaling behaviour of the constants C_2^{LSF} and C_2^{TSF} can be reasonably explained by a simple two-state model (Davidson 2004; Monin & Yaglom 2007), which is based on Kolmogorov's universal equilibrium theory. The behaviour of higher even-order structure functions (i.e. the fourth- and sixth-order) was also investigated. Numerical results indicate that the distributions of the conditional higher-order structure functions deviate from self-similarity due to the significant effect of the TNTI blocking/sheltering mechanism. We further found that the conditional higher-order structure functions recover self-similarity after excluding the turbulent region near the TNTI.

The self-similarity analysis based on the Kármán–Howarth equation shows that the conditional third-order structure functions at different cross-wise positions collapse

https://doi.org/10.1017/jfm.2026.11642 Published online by Cambridge University Press

reasonably within the small-scale dissipation range where the unsteady term $I_u^*(r)$ can be neglected. The numerical results are found to be in good agreement with the self-similarity analysis. However, the conditional third-order structure function deviates from self-similarity in the inertial range. This is related to the fact that the contribution of $I_u^*(\lambda^T)$ in the intermittent region with $\gamma = 0.5$ is greater than that in the fully turbulent region with $\gamma = 1.0$. For a higher Reynolds number Re_H, the range of self-similarity extends to increasingly larger values of r/η^T. Considering that the contribution of $I_u^*(r)$ within the inertial range gradually decreases with increasing Re_λ^T, it is expected that the self-similar behaviour of the third-order structure function will be recovered at sufficiently high Reynolds numbers.

An empirical formula for $\langle \delta u'^n \rangle(r)$ is used to investigate the FRN effect on the structure functions. The numerical results show good agreement with the empirical formula at small and intermediate scales, which makes it possible to extrapolate the current findings to higher Reynolds numbers. For the fully turbulent region with $\gamma = 1.0$, the extrapolated results indicate that the FRN effect may differ between the second- and third-order structure functions. To satisfy the Kolmogorov K41 scaling, i.e. $\langle \delta u'^n \rangle(r) \sim r^{n/3}$, the third-order structure function may require a much higher Re_λ^T than the second-order structure function. For the intermittent region with $\gamma = 0.5$, the conditional structure function may satisfy Kolmogorov's K41 scaling despite the strong anisotropy of the flow. However, compared with the fully turbulent region, establishing Kolmogorov's K41 scaling in the intermittent region with $\gamma = 0.5$ requires a much higher Re_λ^T. More specifically, for the conditional second- and third-order structure functions in the intermittent region, the values of Re_λ^T need to reach approximately 10^4 and 10^5, respectively, whereas in the fully turbulent region, the corresponding values are approximately 8×10^3 and 4×10^4. This indicates that the conditional third-order structure function profiles recover self-similarity at intermediate scales when the local Reynolds number based on the Taylor microscale exceeds 10^5, since the contribution of unsteady terms at these scales can be neglected. Clearly, further investigation is required to understand the FRN effect on the structure functions in the intermittent region and to evaluate the applicability of the K41 theory by further increasing Re_λ^T.

The applicability of our current findings to other types of turbulence, such as turbulent boundary layers, remains an important question for future research. A recent parallel study indicates that the emergence of the $2/3$ scaling law of the second-order structure function is closely related to the uniform momentum zones in the boundary layer (Heisel *et al.* 2022). Another pertinent question is the behaviour of structure functions within the framework of uniform momentum zones (Meinhart & Adrian 1995; de Silva, Hutchins & Marusic 2016). In this framework, turbulent flows can be approximated as a series of regions with relatively uniform streamwise velocity. Different uniform momentum zones can be regarded as different flow states, where the behaviour of the second-order structure function needs to be addressed through further research.

Acknowledgements. The DNS presented in this paper was performed using the high-performance computing system in the Japan Agency for Marine-Earth Science and Technology. Part of the work was carried out under the Collaborative Research Project of the Institute of Fluid Science, Tohoku University, with additional computational resources provided by the Hefei advanced computing center.

Funding. This study was co-supported by the National Natural Science Foundation of China (Nos. 12472223 and 52306249), 2024 Jiangsu Provincial Carbon Peaking and Carbon Neutrality Science and Technology Innovation Special Project (No. BT2024003), the Fundamental Research Funds for Central Universities (No. 30924010923), and JSPS KAKENHI (Grant No. JP23K22669).

Declaration of interests. The authors report no conflict of interest.

https://doi.org/10.1017/jfm.2026.11642 Published online by Cambridge University Press

Appendix A. Two-state model and self-similarity analysis of structure functions

Landau was the first to recognise the role of large-scale fluctuations, suggesting that large-scale fluctuations in the dissipation field can destroy the universality of small-scale statistics (Landau & Lifshits 1944). Davidson (2004) and Monin & Yaglom (2007) proposed a simple two-state model based on Kolmogorov's universal equilibrium theory to predict the behaviour of structure functions. It was qualitatively shown that the Kolmogorov constant in the inertial range is significantly influenced by large-scale fluctuations. The two-state model significantly simplifies the complex multiscale turbulent flow by considering only two distinct turbulent states: the strong dissipation state (state I, $\varepsilon_1 = (1+\beta)\varepsilon$) and the weak dissipation state (state II, $\varepsilon_2 = (1-\beta)\varepsilon$). Here, β represents the magnitude of the difference in energy dissipation between two different states. When considering unequal occurrence probabilities for states I and II, denoted by γ and $1-\gamma$, respectively, ε_1 and ε_2 satisfy the relationship with the actual energy dissipation rate ε: $\gamma\varepsilon_1 + (1-\gamma)\varepsilon_2 = \varepsilon$. The corresponding energy dissipation rates for states I and II are given by $\varepsilon_1 = (1+(1-\gamma)\beta/\gamma)\varepsilon$ and $\varepsilon_2 = (1-\beta)\varepsilon$, respectively. For this extended model, the nth-order longitudinal structure function can be expressed as (Chien *et al.* 2013)

$$\langle \delta u'^n \rangle(r) = \kappa_n(\beta, \gamma) C_n^{LSF} (\varepsilon r)^{n/3}, \tag{A1}$$

where

$$\kappa_n(\beta, \gamma) = \left[\gamma \left(1 + \frac{1-\gamma}{\gamma}\beta \right)^{n/3} + (1-\gamma)(1-\beta)^{n/3} \right] \tag{A2}$$

represents the modification to the Kolmogorov constant C_n^{LSF} due to the effect of large-scale fluctuations. Large-scale intermittency is closely related to large-scale fluctuations in energy dissipation. External intermittency is an extreme case of large-scale intermittency, originating from the highly distorted TNTI. Admittedly, the turbulent and laminar regions separated by the TNTI represent an extreme case of two completely different flow states. The dissipation in the laminar region is negligible and the contained fluid has no enstrophy. Large-scale fluctuations in the energy dissipation field caused by strong inhomogeneity and anisotropy are expected to modify the scaling law of the Kolmogorov constant C_n^{LSF} in the inertial range, as predicted by (A2). In the extreme case, we have $\beta = 1$. Consequently, the energy dissipation rates corresponding to states I and II are $\varepsilon_1 = \gamma^{-1}\varepsilon$ and $\varepsilon_2 = 0$, respectively.

For even-order structure functions $\langle \delta u'^n \rangle(r)$, the correction parameter $\kappa_n(\beta, \gamma)$ is given by

$$\kappa_n(\beta, \gamma) = \gamma^{(3-n)/3}. \tag{A3}$$

This implies that the Kolmogorov constant C_n^{LSF} follows a power-law relationship with the intermittency factor γ. The derivation results directly support the scaling laws of the Kolmogorov constants C_2^{LSF} and C_2^{TSF} in the intermittent region, namely, $C_2^{LSF} \sim \gamma^{1/3}$ and $C_2^{TSF} \sim \gamma^{1/3}$. Similarly, for the third-order structure function $\langle \delta u'^3 \rangle(r)$, we have $\kappa_3(\beta, \gamma) = 1$. This means that the Kolmogorov constant C_3^{LSF} is unaffected by the external intermittency. Considering that ε^L can be ignored in the laminar region, that is, $\varepsilon \approx \gamma\varepsilon^T$, substituting it into (A1) can obtain the conditional structure function of the turbulent region, which can be expressed as

$$\langle \delta u'^n \rangle(r) = \gamma C_n^{LSF} \left(\varepsilon^T r \right)^{n/3}. \tag{A4}$$

https://doi.org/10.1017/jfm.2026.11642 Published online by Cambridge University Press

For $n = 2$, this is consistent with the self-similar form of the conditional second-order structure function, i.e. (3.1).

Appendix B. Statistical convergence of structure functions

To ensure the convergence of the statistical results for the structure functions, the DNS is repeated N_S times for each Reynolds number Re_H using different initial velocity perturbations. For Reynolds numbers $Re_H = 10^4$ and 10^5, N_S was 6 and 1, respectively. It is important to emphasise that for two different Reynolds numbers ($Re_H = 10^4$ and 10^5), the corresponding total numbers of grid points reach approximately 6 billion and 82 billion, respectively. The repeated simulations together with the large total number of grid points provide confidence in the convergence of the statistical results.

The error bars and statistical convergence of the structure functions at $\gamma = 0.5$ for $Re_H = 10^4$ were examined. Figure 21(a) shows the error bars of structure functions up to the sixth order at $\gamma = 0.5$. The estimates for the error bars are derived from six subsamples, computed after dividing the dataset into six subsamples. As the order increases from second to sixth, the statistical error of the structure function becomes progressively larger. This is likely attributable to a reduction of statistical samples, leading to a lack of statistical convergence. Therefore, these error bars should be interpreted only as a qualitative indication of the variability among subsamples, rather than as a rigorous confidence interval. Conversely, a more appropriate approach is to validate the reliability and robustness of statistical measures through tests of statistical convergence. Figure 21(b) shows the statistical convergence of structure functions up to the sixth order at $\gamma = 0.5$ and $Re_H = 10^4$. The statistical results of the second-order structure functions show good convergence. For higher-order structure functions, the situation is more challenging and their convergence requires careful examination. The results show that for the sixth-order structure functions, the convergence remains good at small and intermediate scales when the statistical sampling is limited, with the largest deviations occurring at the large scale $r/\eta = 170$. Statistical convergence is satisfactory when using 36 slices to calculate the profile of the structure function. Specifically, for the intermittent region with $\gamma = 0.5$ in each repeated case, we used data from the X–Z plane at $\gamma = 0.5$ and from the adjacent planes above and below. In addition, the third-order structure function distribution in the central plane of the jet shows good agreement with DNS results for grid turbulence at Reynolds number $Re_\lambda = 100$ (Antonia & Burattini 2006). This implies that well-converged results are also obtained for the third-order structure function (see figure 13).

The statistical convergence of the structure functions at $\gamma = 0.5$ for $Re_H = 10^5$ is plotted in figure 22. For the higher Reynolds number $Re_H = 10^5$, the case is slightly more complicated. When only data from 6 slices of the X–Z plane were used, the second-order and fourth-order structure functions showed good statistical convergence. However, the statistical convergence of the third-order and sixth-order structure functions is relatively poor. To this end, we included data from 12 additional slices, resulting in a total of 18 slices, to compute the structure functions in the intermittent regions. Specifically, for the intermittent region at $\gamma = 0.5$, we used data from the X–Z plane at $\gamma = 0.5$ as well as from four planes above and four planes below it. All structure functions show good statistical convergence with increased statistical sampling. Figures 21 and 22 also show that even with further increases in statistical sampling, the statistical results of the structure function hardly change. Overall, satisfactory convergence is observed for the structure function profiles computed from 36 and 18 slices of the X–Z plane for the two Reynolds numbers, respectively.

https://doi.org/10.1017/jfm.2026.11642 Published online by Cambridge University Press

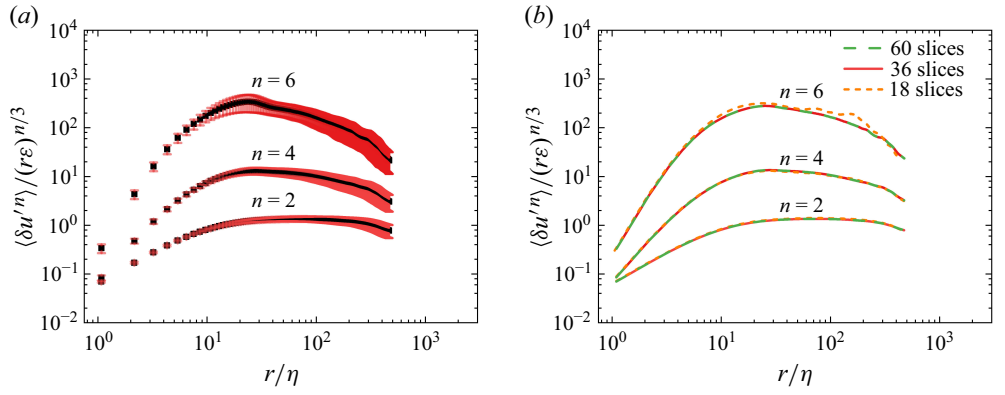


Figure 21. (*a*) Illustration of the error bars of structure functions up to the sixth order at $\gamma = 0.5$ for $Re_H = 10^4$. The error bars corresponding to the black squares represent the standard deviation of the structure functions computed after dividing the dataset into six subsamples. (*b*) Statistical convergence of structure functions up to the sixth order at $\gamma = 0.5$. Statistical results of the structure functions computed using 60 (dashed lines), 36 (solid lines) and 18 (dash-dotted lines) slices of the X–Z plane.

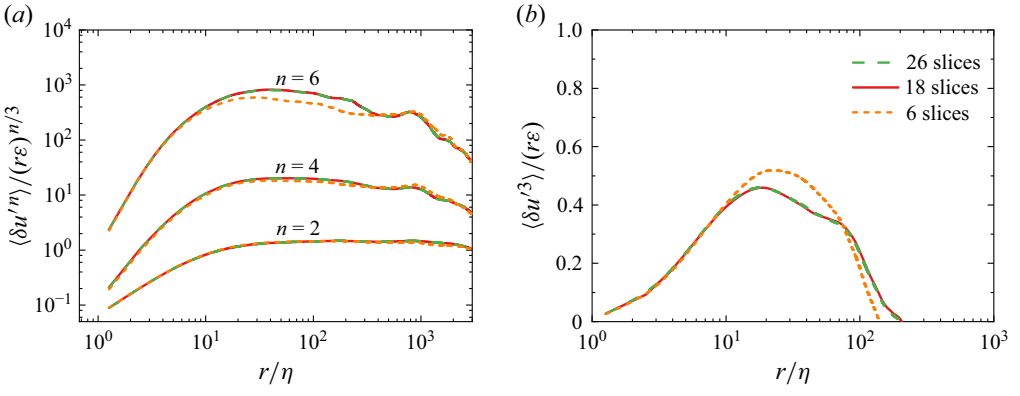


Figure 22. (*a*) Same as figure 21(*b*), but for $Re_H = 10^5$. (*b*) Statistical convergence of the third-order structure function at $\gamma = 0.5$ for $Re_H = 10^5$. Statistical results of the structure functions computed using 26 (dashed lines), 18 (solid lines) and 6 (dash-dotted lines) slices of the X–Z plane.

Appendix C. Connecting the second-order structure function to third-order structure function

Before conducting the self-similarity analysis, we first briefly evaluated the local isotropy of the flow. According to the local isotropic assumption, the longitudinal and transverse second-order structure functions in the streamwise direction are given by the following relationship (Comte-Bellot 1971; Monin & Yaglom 2007; Antonia *et al.* 2017):

$$\langle \delta v'^2 \rangle_{iso}(r) = \left(1 + \frac{r}{2}\frac{\mathrm{d}}{\mathrm{d}r}\right) \langle \delta u'^2 \rangle(r), \tag{C1}$$

where $\delta u'(r) = u'(\boldsymbol{x} + r\boldsymbol{e}_1) - u'(\boldsymbol{x})$. It is necessary to verify local isotropy in the normal direction since the flow in the normal direction is not strictly homogeneous. Similarly, the local isotropy relationship between $\langle \delta u'^2 \rangle(r)$ and $\langle \delta v'^2 \rangle(r)$ in the normal direction can be

https://doi.org/10.1017/jfm.2026.11642 Published online by Cambridge University Press

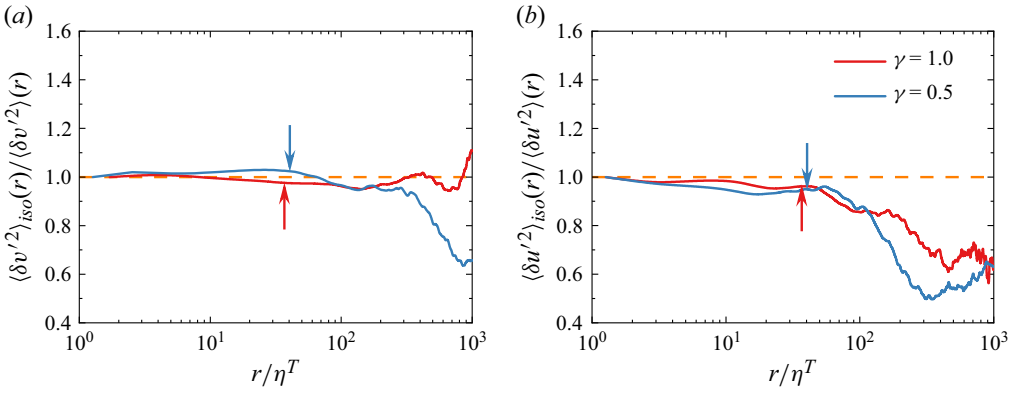


Figure 23. Ratio of isotropic prediction to calculated transverse structure function for $Re_H = 10^5$. (*a*) $\langle \delta v'^2 \rangle_{iso}(r)/\langle \delta v'^2 \rangle(r)$; (*b*) $\langle \delta u'^2 \rangle_{iso}(r)/\langle \delta u'^2 \rangle(r)$. Note that the separation distance r in panels (*a*) and (*b*) corresponds to the distances in the streamwise and normal directions, respectively. The horizontal dashed line indicates the isotropic ratio of 1. The vertical arrows indicate the locally isotropic values at $r = \lambda^T$ for two different cross-wise positions.

expressed as

$$\langle \delta u'^2 \rangle_{iso}(r) = \left(1 + \frac{r}{2}\frac{\mathrm{d}}{\mathrm{d}r}\right)\langle \delta v'^2 \rangle(r), \tag{C2}$$

where $\delta v'(r) = v'(\boldsymbol{x} + r\boldsymbol{e}_2) - v'(\boldsymbol{x})$. Here, $\boldsymbol{e}_1$ and $\boldsymbol{e}_2$ are the unit vectors in the streamwise and normal directions, respectively. Note that the separation distance r in (C1) and (C2) corresponds to the distances in the streamwise and normal directions, respectively. Following Comte-Bellot (1971) and Antonia *et al.* (2017), the local isotropy of the flow at each scale is checked by using the dynamical relationship between the longitudinal and transverse structure functions, i.e. (C1) and (C2). Tang *et al.* (2017) examined local isotropy at each scale along the axis of the plane jet using (C1) and found that the deviation from local isotropy was less than 20 % when $r < \lambda^T$. The ratios between the isotropic predictions and the calculated transverse structure functions in the streamwise and normal directions at $Re_H = 10^5$, i.e. $\langle \delta v'^2 \rangle_{iso}(r)/\langle \delta v'^2 \rangle(r)$ and $\langle \delta u'^2 \rangle_{iso}(r)/\langle \delta u'^2 \rangle(r)$, are plotted in figure 23. A similar observation was reported by Kitamura *et al.* (2014), although their analysis was based on the autocorrelation function of velocity fluctuations, i.e. $g(r) = f(r) + r\,\mathrm{d}f(r)/(2\,\mathrm{d}r)$, where $f(r) = \langle u(\boldsymbol{x})u(\boldsymbol{x} + r\boldsymbol{e}_1)\rangle/\langle u(\boldsymbol{x})^2\rangle$ and $g(r) = \langle v(\boldsymbol{x})v(\boldsymbol{x} + r\boldsymbol{e}_1)\rangle/\langle v(\boldsymbol{x})^2\rangle$. As shown in figure 23(*a*), the deviation from local isotropy is less than 3 % in the streamwise direction at $r = \lambda^T$. The ratio is 0.980 and 1.024 at $\gamma = 1.0$ and 0.5, respectively. The deviation from local isotropy at $r = \lambda^T$ is approximately 5 % in the normal direction, which is slightly larger than that in the streamwise direction (see figure 23*b*). Notably, the satisfactory collapse of the conditional second-order structure function profiles also implies that the turbulence in the intermittent region exhibits a similar degree of local isotropy to that in the fully turbulent region (see figures 6*b* and 8*b*). The approximate local isotropy at $r \leqslant \lambda_T$ implies that the general form of the Kármán–Howarth equation (i.e. (4.1)) applies not only to fully turbulent flows but also to turbulence in intermittent regions, at least over this range of scales.

The primary focus here is to investigate the conditions for the existence of self-similar solutions to (4.1) when normalised by the conditional Kolmogorov length scale. When the contribution of $I_u(r)$ within the inertial range is neglected at sufficiently high Reynolds numbers, then substituting the self-similar expression (3.1) into (4.1), the following

https://doi.org/10.1017/jfm.2026.11642 Published online by Cambridge University Press

relationship can be obtained:

$$-\langle \delta u'^3 \rangle(\zeta)/\left(\gamma v_\eta^{T3}\right) = \frac{4}{5}\zeta \varepsilon^T \eta^T / v_\eta^{T3} - 6\frac{\nu}{v_\eta^T \eta^T}\frac{\partial}{\partial \zeta}\langle \delta u'^2 \rangle(\zeta)/\left(\gamma v_\eta^{T2}\right) = h(\zeta). \quad \text{(C3)}$$

By applying the scaling laws for ε^T, η^T and v_η^T, i.e. $\varepsilon^T \approx \gamma^{-1}\varepsilon$, $\eta^T \approx \gamma^{1/4}\eta$ and $v_\eta^T \approx \gamma^{-1/4} v_\eta$ (Zhou *et al.* 2023), it is evident that the two dimensionless parameters may be similarity solutions to the equation, since $\varepsilon^T \eta^T / v_\eta^{T3}$ and $\nu/(v_\eta^T \eta^T)$ are constants, that is,

$$\frac{\varepsilon^T \eta^T}{v_\eta^{T3}} = \frac{\varepsilon \eta}{v_\eta^3} = 1 \quad \text{and} \quad \frac{\nu}{v_\eta^T \eta^T} = \frac{\nu}{v_\eta \eta} = \frac{1}{Re_\eta} = 1. \quad \text{(C4)}$$

Accordingly, one may reasonably conclude that self-similar solutions are always valid at sufficiently high Reynolds numbers since the two dimensionless parameters remain constant. In other words, at sufficiently high Reynolds numbers, the distribution of the conditional third-order structure function exhibits self-similarity for different cross-wise positions with different intermittency factor.

References

Alves Portela, F., Papadakis, G. & Vassilicos, J.C. 2017 The turbulence cascade in the near wake of a square prism. *J. Fluid Mech.* **825**, 315–352.

Antonia, R.A. & Burattini, P. 2006 Approach to the 4/5 law in homogeneous isotropic turbulence. *J. Fluid Mech.* **550**, 175–184.

Antonia, R.A., Djenidi, L., Danaila, L. & Tang, S.L. 2017 Small scale turbulence and the finite Reynolds number effect. *Phys. Fluids* **29** (2), 020715.

Antonia, R.A., Tang, S.L., Danaila, L., Djenidi, L. & Zhou, Y. 2019*a* K41 versus K62: Recent developments. In *Fluid-Structure-Sound Interactions and Control: Proceedings of the 4th Symposium on Fluid-Structure-Sound Interactions and Control*, pp. 3–14. Springer.

Antonia, R.A., Tang, S.L., Djenidi, L. & Zhou, Y. 2019*b* Finite Reynolds number effect and the 4/5 law. *Phys. Rev. Fluids* **4** (8), 084602.

Belin, F., Maurer, J., Tabeling, P. & Willaime, H. 1997 Velocity gradient distributions in fully developed turbulence: an experimental study. *Phys. Fluids* **9** (12), 3843–3850.

Blum, D.B., Bewley, G.P., Bodenschatz, E., Gibert, M., Gylfason, A., Mydlarski, L., Voth, G.A., Xu, H. & Yeung, P.K. 2011 Signatures of non-universal large scales in conditional structure functions from various turbulent flows. *New J. Phys.* **13** (11), 113020.

Chien, C.C., Blum, D.B. & Voth, G.A. 2013 Effects of fluctuating energy input on the small scales in turbulence. *J. Fluid Mech.* **737**, 527–551.

Comte-Bellot, G. & Corrsin, S. 1971 Simple Eulerian time correlation of full-and narrow-band velocity signals in grid-generated,'isotropic'turbulence. *J. Fluid Mech.* **48** (2), 273–337.

Corrsin, S. 1958 Local isotropy in turbulent shear flow. *NACA Tech. Rep. RM* 58B11.

da Silva, C.B., Hunt, J.C.R., Eames, I. & Westerweel, J. 2014 Interfacial layers between regions of different turbulence intensity. *Annu. Rev. Fluid Mech.* **46**, 567–590.

da Silva, C.B. & Pereira, J. 2008 Invariants of the velocity-gradient, rate-of-strain, and rate-of-rotation tensors across the turbulent/nonturbulent interface in jets. *Phys. Fluids* **20** (5), 055101.

Danaila, L., Anselmet, F., Zhou, T. & Antonia, R.A. 1999 A generalization of Yaglom's equation which accounts for the large-scale forcing in heated decaying turbulence. *J. Fluid Mech.* **391**, 359–372.

Danaila, L., Anselmet, F., Zhou, T. & Antonia, R.A. 2001 Turbulent energy scale budget equations in a fully developed channel flow. *J. Fluid Mech.* **430**, 87–109.

Davidson, P.A. 2004 *Turbulence, An Introduction for Scientists and Engineers*. Oxford University Press.

Dhruva, B.R. 2000 An experimental study of high Reynolds number turbulence in the atmosphere. PhD thesis, Yale University.

Dhruva, B., Tsuji, Y. & Sreenivasan, K.R. 1997 Transverse structure functions in high-Reynolds-number turbulence. *Phys. Rev. E* **56** (5), R4928–R4930.

Er, S., Laval, J.-P. & Vassilicos, J.C. 2023 Length scales and the turbulent/non-turbulent interface of a temporally developing turbulent jet. *J. Fluid Mech.* **970**, A33.

https://doi.org/10.1017/jfm.2026.11642 Published online by Cambridge University Press

GAUDING, M., BODE, M., BRAHAMI, Y., VAREA, É. & DANAILA, L. 2021 Self-similarity of turbulent jet flows with internal and external intermittency. *J. Fluid Mech.* **919**, A41.
GRAUER, R., HOMANN, H. & PINTON, J. 2012 Longitudinal and transverse structure functions in high-Reynolds-number turbulence. *New J. Phys.* **14** (6), 063016.
HAYASHI, M., WATANABE, T. & NAGATA, K. 2021 Characteristics of small-scale shear layers in a temporally evolving turbulent planar jet. *J. Fluid Mech.* **920**, A38.
HEISEL, M., DE SILVA, C.M., KATUL, G.G. & CHAMECKI, M. 2022 Self-similar geometries within the inertial subrange of scales in boundary layer turbulence. *J. Fluid Mech.* **942**, A33.
HILL, R.J. 2001 Equations relating structure functions of all orders. *J. Fluid Mech.* **434**, 379–388.
HUNT, J.C.R. & DURBIN, P.A. 1999 Perturbed vortical layers and shear sheltering. *Fluid Dyn. Res.* **24**, 375–404.
ISHIHARA, T., GOTOH, T. & KANEDA, Y. 2009 Study of high–Reynolds number isotropic turbulence by direct numerical simulation. *Annu. Rev. Fluid Mech.* **41** (1), 165–180.
ISHIHARA, T., MORISHITA, K., YOKOKAWA, M., UNO, A. & KANEDA, Y. 2016 Energy spectrum in high-resolution direct numerical simulations of turbulence. *Phys. Rev. Fluids* **1** (8), 082403.
IYER, K.P., SREENIVASAN, K.R. & YEUNG, P.K. 2017 Reynolds number scaling of velocity increments in isotropic turbulence. *Phys. Rev. E* **95** (2), 021101.
KANEDA, Y., YOSHINO, J. & ISHIHARA, T. 2008 Examination of Kolmogorov's 4/5 law by high-resolution direct numerical simulation data of turbulence. *J. Phys. Soc. Japan* **77** (6), 064401.
KERR, R.M. 1985 Higher-order derivative correlations and the alignment of small-scale structures in isotropic numerical turbulence. *J. Fluid Mech.* **153**, 31–58.
KITAMURA, T., NAGATA, K., SAKAI, Y., SASOH, A., TERASHIMA, O., SAITO, H. & HARASAKI, T. 2014 On invariants in grid turbulence at moderate Reynolds numbers. *J. Fluid Mech.* **738**, 378–406.
KOLMOGOROV, A.N. 1941*a* Dissipation of energy in the locally isotropic turbulence. *Dokl. Akad. Nauk SSSR* **32**, 16–18.
KOLMOGOROV, A.N. 1941*b* The local structure of turbulence in incompressible viscous fluid for very large Reynolds numbers. *Dokl. Akad. Nauk SSSR* **30**, 301–305.
KOLMOGOROV, A.N. 1941*c* On the degeneration of isotropic turbulence in an incompressible viscous fluid. *Dokl. Akad. Nauk SSSR* **31**, 538–540.
KOLMOGOROV, A.N. 1962 A refinement of previous hypotheses concerning the local structure of turbulence in a viscous incompressible fluid at high Reynolds number. *J. Fluid Mech.* **13**, 82–85.
KOVASZNAY, L.S.G., KIBENS, V. & BLACKWELDER, R.F. 1970 Large-scale motion in the intermittent region of a turbulent boundary layer. *J. Fluid Mech.* **41** (2), 283–325.
KURIEN, S. & SREENIVASAN, K.R. 2000 Anisotropic scaling contributions to high-order structure functions in high-Reynolds-number turbulence. *Phys. Rev. E* **62** (2), 2206.
KUZNETSOV, V.R., PRASKOVSKY, A.A. & SABELNIKOV, V.A. 1992 Fine-scale turbulence structure of intermittent hear flows. *J. Fluid Mech.* **243**, 595–622.
LAIZET, S., VASSILICOS, J.C. & CAMBON, C. 2013 Interscale energy transfer in decaying turbulence and vorticity-strain-rate dynamics in grid-generated turbulence. *Fluid Dyn. Res.* **45**, 061408.
LANDAU, L.D. & LIFSHITS, E.M. 1944 *Fluid Mechanics (in Russian) USSR*. (Also 2nd edition, Pergamon Press, 1987).
LARUE, J.C. & LIBBY, P.A. 1976 Statistical properties of the interface in the turbulent wake of a heated cylinder. *Phys. Fluids* **19** (12), 1864–1875.
LAWSON, J.M., BODENSCHATZ, E., KNUTSEN, A.N., DAWSON, J.R. & WORTH, N.A. 2019 Direct assessment of Kolmogorov's first refined similarity hypothesis. *Phys. Rev. Fluids* **4**, 022601.
MEINHART, C.D. & ADRIAN, R.J. 1995 On the existence of uniform momentum zones in a turbulent boundary layer. *Phys. Fluids* **7** (4), 694–696.
MONIN, A.S. & YAGLOM, A.M. 2007 *Statistical Fluid Mechanics*, Mechanics of Turbulence, vol. II. Dover Publications.
MORINISHI, Y., LUND, T.S., VASILYEV, O.V. & MOIN, P. 1998 Fully conservative higher order finite difference schemes for incompressible flow. *J. Comput. Phys.* **143**, 90–124.
NAGARAJAN, S., LELE, S.K. & FERZIGER, J.H. 2003 A robust high-order compact method for large eddy simulation. *J. Comput. Phys.* **191** (2), 392–419.
OBUKHOV, A.M. 1962 Some specific features of atmospheric turbulence. *J. Fluid Mech.* **13**, 77–81.
PEARSON, B.R. & ANTONIA, R.A. 2001 Reynolds-number dependence of turbulent velocity and pressure increments. *J. Fluid Mech.* **444**, 343–382.
POPE, S.B. 2000 *Turbulent Flows*. Cambridge University Press.
REUTHER, N. & KÄHLER, C.J. 2020 Effect of the intermittency dynamics on single and multipoint statistics of turbulent boundary layers. *J. Fluid Mech.* **897**, A11.

https://doi.org/10.1017/jfm.2026.11642 Published online by Cambridge University Press

ROSA, R. 2026 Energy cascade for cross-shear length scales in free-shear three-dimensional incompressible viscous flows. arXiv preprint arXiv: 2603.14626.
SADDOUGHI, S.G. & VEERAVALLI, S.V. 1994 Local isotropy in turbulent boundary layers at high Reynolds number. *J. Fluid Mech.* **268**, 333–372.
SADEGHI, H., LAVOIE, P. & POLLARD, A. 2015 Equilibrium similarity solution of the turbulent transport equation along the centreline of a round jet. *J. Fluid Mech.* **772**, 740–755.
SCHUMACHER, J., SREENIVASAN, K.R. & YAKHOT, V. 2007 Asymptotic exponents from low-Reynolds-number flows. *New J. Phys.* **9**, 89.
SHEN, X. & WARHAFT, Z. 2002 Longitudinal and transverse structure functions in sheared and unsheared wind-tunnel turbulence. *Phys. Fluids* **14** (1), 370–381.
DE SILVA, C.M., HUTCHINS, N. & MARUSIC, I. 2016 Uniform momentum zones in turbulent boundary layers. *J. Fluid Mech.* **786**, 309–331.
SREENIVASAN, K.R. 1991 Fractals and multifractals in fluid turbulence. *Annu. Rev. Fluid Mech.* **23** (1), 539–604.
SREENIVASAN, K.R. & ANTONIA, R.A. 1997 The phenomenology of small-scale turbulence. *Annu. Rev. Fluid Mech.* **29**, 435–472.
SREENIVASAN, K.R. & DHRUVA, B. 1998 Is there scaling in high-Reynolds-number turbulence? *Prog. Theor. Phys. Suppl.* **130**, 103–120.
STOLOVITZKY, G., KAILASNATH, P. & SREENIVASAN, K.R. 1992 Kolmogorov's refined similarity hypotheses. *Phys. Rev. Lett.* **69**, 1178.
STOLOVITZKY, G. & SREENIVASAN, K.R. 1994 Kolmogorov refined similarity hypotheses for turbulence and general stochastic-processes. *Rev. Mod. Phys.* **66**, 229.
SUZUKI, H., NAGATA, K., SAKAI, Y., HAYASE, T., HASEGAWA, Y. & USHIJIMA, T. 2013 An attempt to improve accuracy of higher-order statistics and spectra in direct numerical simulation of incompressible wall turbulence by using the compact schemes for viscous terms. *Intl J. Numer. Meth. Fluids* **73** (6), 509–522.
TABELING, P., ZOCCHI, G., BELIN, F., MAURER, J. & WILLAIME, H. 1996 Probability density functions, skewness, and flatness in large Reynolds number turbulence. *Phys. Rev. E* **53** (2), 1613.
TANG, S.L., ANTONIA, R.A. & DJENIDI, L. 2023 Dual scaling and the n-thirds law in grid turbulence. *J. Fluid Mech.* **975**, A32.
TANG, S.L., ANTONIA, R.A., DJENIDI, L., DANAILA, L. & ZHOU, Y. 2017 Finite Reynolds number effect on the scaling range behaviour of turbulent longitudinal velocity structure functions. *J. Fluid Mech.* **820**, 341–369.
TANG, S.L., ANTONIA, R.A., DJENIDI, L. & ZHOU, Y. 2019 *Phys. Rev. Fluids* **4** (2), 024607.
THIESSET, F., ANTONIA, R.A. & DJENIDI, L. 2014 Consequences of self-preservation on the axis of a turbulent round jet. *J. Fluid Mech.* **748**, R2.
TOWNSEND, A.A. 1951 On the fine-scale structure of turbulence. *Proc. R. Soc. A* **208** (1095), 534–542.
TSUJI, Y. & ISHIHARA, T. 2003 Similarity scaling of pressure fluctuation in turbulence. *Phys. Rev. E* **68** (2), 026309.
VAN ATTA, C.W. & ANTONIA, R.A. 1980 Reynolds number dependence of skewness and flatness factors of turbulent velocity derivatives. *Phys. Fluids* **23** (2), 252–257.
VAN REEUWIJK, M., VASSILICOS, J.C. & CRASKE, J. 2021 Unified description of turbulent entrainment. *J. Fluid Mech.* **908**, A12.
WANG, L.P., CHEN, S.Y., BRASSEUR, J.G. & WYNGAARD, J.C. 1996 Examination of hypotheses in the Kolmogorov refined turbulence theory through high-resolution simulations. Part 1. Velocity field. *J. Fluid Mech.* **309**, 113–156.
WANG, L. & FU, S. 2011 Development of an intermittency equation for the modeling of the supersonic/hypersonic boundary layer flow transition. *Flow Turbul. Combust.* **87**, 165–187.
WATANABE, T., RILEY, J.J., NAGATA, K., ONISHI, R. & MATSUDA, K. 2018*a* A localized turbulent mixing layer in a uniformly stratified environment. *J. Fluid Mech.* **849**, 245–276.
WATANABE, T., SILVA, C.B.D. & NAGATA, K. 2019*a* Non-dimensional energy dissipation rate near the turbulent/non-turbulent interfacial layer in free shear flows and shear free turbulence. *J. Fluid Mech.* **875**, 321–344.
WATANABE, T., ZHANG, X.X. & NAGATA, K. 2018*b* Turbulent/non-turbulent interfaces detected in DNS of incompressible turbulent boundary layers. *Phys. Fluids* **30** (3), 035102.
WATANABE, T., ZHANG, X. & NAGATA, K. 2019*b* Direct numerical simulation of incompressible turbulent boundary layers and planar jets at high Reynolds numbers initialized with implicit large eddy simulation. *Comput. Fluids* **194**, 104314.

https://doi.org/10.1017/jfm.2026.11642 Published online by Cambridge University Press

XIE, H.S., QI, H., XIAO, M.J., ZHANG, Y.S. & ZHAO, Y.M. 2025*a* An intermittency based Reynolds-averaged transition model for mixing flows induced by interfacial instabilities. *J. Fluid Mech.* **1002**, A31.

XIE, Y.L., XIONG, X., ZHENG, Y.L., NAGATA, K., WATANABE, T. & ZHOU, Y. 2025*b* Scaling law of the Kolmogorov constants in turbulent flow with external intermittency. *J. Fluid Mech. Accept.* **1019**, A30.

XIE, Y.L., ZHANG, X.X., XIONG, X. & ZHOU, Y. 2024 Temporal evolution of the turbulence interface of a turbulent plane jet. *J. Fluid Mech.* **1001**, A39.

YAO, H., YEUNG, P.K., ZAKI, T.A. & MENEVEAU, C. 2024 Forward and inverse energy cascade in fluid turbulence adhere to Kolmogorov's refined similarity hypothesis. *Phys. Rev. Lett.* **132** (16), 164001.

YEUNG, P.K., RAVIKUMAR, K., UMA-VAIDESWARAN, R., DOTSON, D.L., SREENIVASAN, K.R., POPE, S.B., MENEVEAU, C. & NICHOLS, S. 2025 Small-scale properties from exascale computations of turbulence on a periodic cube. *J. Fluid Mech.* **1019**, R2.

ZECCHETTO, M. & DA SILVA, C.B. 2021 Universality of small-scale motions within the turbulent/non-turbulent interface layer. *J. Fluid Mech.* **916**, A9.

ZHANG, X.X., WATANABE, T. & NAGATA, K. 2018 Turbulent/nonturbulent interfaces in high-resolution direct numerical simulation of temporally evolving compressible turbulent boundary layers. *Phys. Rev. Fluids* **3** (9), 094605.

ZHANG, X.X., WATANABE, T. & NAGATA, K. 2023 Reynolds number dependence of the turbulent/non-turbulent interface in temporally developing turbulent boundary layers. *J. Fluid Mech.* **964**, A8.

ZHOU, T. & ANTONIA, R.A. 2000 Reynolds number dependence of the small-scale structure of grid turbulence. *J. Fluid Mech.* **406**, 81–107.

ZHOU, Y., NAGATA, K., ITO, Y., SAKAI, Y. & HAYASE, T. 2023 Appearance of the $-5/3$ scaling law in spatially intermittent flows with strong vortex shedding. *Phys. Fluids* **35**, 045116.

ZHOU, Y., NAGATA, K., SAKAI, Y., ITO, Y. & HAYASE, T. 2016 Spatial evolution of the helical behavior and the 2/3 power-law in single-square-grid-generated turbulence. *Fluid Dyn. Res.* **48** (2), 021404.

ZHOU, Y., NAGATA, K., SAKAI, Y. & WATANABE, T. 2019 Extreme events and non-Kolmogorov $-5/3$ spectra in turbulent flows behind two side-by-side square cylinders. *J. Fluid Mech.* **874**, 677–698.

ZHOU, Y., NAGATA, K., SAKAI, Y., WATANABE, T., ITO, Y. & HAYASE, T. 2020 Energy transfer in turbulent flows behind two side-by-side square cylinders. *J. Fluid Mech.* **903**, A4.

https://doi.org/10.1017/jfm.2026.11642 Published online by Cambridge University Press